Superinductive Ultrastrong Couplings in Superconducting Quantum Circuits

Alba Torras Coloma

Director: Pol Forn-Díaz
Tutora: Marta Gonzalez Silveira

Programa de Doctorat en Física

Universitat Autònoma de Barcelona

Cerdanyola del Vallès, 2025

Contents

1 Introduction and Summary **19**

1.1 Superconducting qubits 20

1.1.1 Types of superconducting qubits 21

1.1.2 Flux qubits 22

1.2 Light-matter interaction in superconducting quantum circuits . . . 26

1.2.1 The Quantum Rabi Model 27

1.2.2 Ultrastrong coupling regime of light-matter interaction . . . 28

1.2.3 Ultrastrong coupling regime with superconducting qubits . 30

1.3 Superinductors 33

1.3.1 Josephson junction arrays 34

1.3.2 Disordered and granular superconductors 35

1.3.3 Superinductors for superconducting quantum circuit applications 38

1.4 Thesis overview 39

2 Experimental methods **41**

2.1 Micro and nanofabrication 41

2.1.1 Microfabrication techniques and recipes 42

2.1.2 Granular aluminum fabrication 45

2.1.3 Qubit and junction fabrication 48

2.2 Experimental setup 58

2.2.1 Room temperature characterization setup 58

2.2.2 Qubit and DC measurement setup 58

3 Superinductive ultrastrong couplings: Theory **63**

3.1 Introduction and description of the system 64

3.2 3-junction flux qubit with a non-negligible loop inductance 65

3.2.1 Criteria for a double-well potential 67

3.3 3-junction flux qubit galvanically coupled to an LC resonator . . . 69

3.3.1 Circuit Hamiltonian derivation 69

3.3.2 Coupling estimate 72

3.3.3 Approximate expressions for the coupling coefficient 76

3.4 Numerical diagonalization methods 81

3.4.1 Standard method 82
3.4.2 Normal modes 83
3.4.3 Comparison between diagonalization methods 86
3.5 Electric dipole moment and emission rate of a flux qubit capacitively coupled to an open waveguide 89
3.5.1 *Scqubits* to estimate the electric dipole moment 91

4 Superinductive ultrastrong couplings: Experiments 95
4.1 Design of a qubit-resonator system in the ultrastrong coupling regime 96
4.1.1 Resonator design 98
4.1.2 Qubit design 100
4.1.3 Coupled system 104
4.2 Spectrum characterization 106
4.2.1 Room temperature and grAl characterization 106
4.2.2 Low-temperature transmission measurements 108
4.2.3 USC spectrum discussion 116
4.3 Outlook 119

5 Superconducting Nitridized-Aluminum thin films 123
5.1 Introduction 124
5.2 Room-temperature properties 126
5.3 Low-temperature properties 126
5.3.1 Temperature-resistance curves 127
5.3.2 Critical temperature of NitrAl 129
5.3.3 Current and magnetic field response 134
5.4 Resonator characterization 136
5.4.1 Sample preparation 137
5.4.2 Resonator measurements 138
5.5 Final remarks 141

6 Conclusions and perspectives 143
6.1 Conclusions 143
6.2 Perspectives 144
6.2.1 USC experiments 144
6.2.2 NitrAl experiments 145

A Fabrication recipes 147
A.1 Substrate cleaning 147
A.2 Optical lithography 147
A.2.1 Positive photoresist - Mask aligner 148
A.2.2 Negative photoresist - Maskless aligner 148
A.3 Vertical Al evaporation and lift-off 149

A.4 Electron beam lithography: Josephson junction and contact fabrication . . . 150
A.4.1 Josephson junction fabrication . . . 150
A.4.2 Fabrication of contacts . . . 154
A.5 Granular Aluminum . . . 155

B Flux qubit-resonator Hamiltonian derivation **157**

C NitrAl fabrication **161**

Bibliography **163**

Chapter 1

Introduction and Summary

Contents

1.1 Superconducting qubits 20
1.1.1 Types of superconducting qubits 21
1.1.2 Flux qubits 22
1.2 Light-matter interaction in superconducting quantum circuits 26
1.2.1 The Quantum Rabi Model 27
1.2.2 Ultrastrong coupling regime of light-matter interaction 28
1.2.3 Ultrastrong coupling regime with superconducting qubits 30
1.3 Superinductors 33
1.3.1 Josephson junction arrays 34
1.3.2 Disordered and granular superconductors 35
1.3.3 Superinductors for superconducting quantum circuit applications 38
1.4 Thesis overview 39

The early developments in the study of light-matter interaction revolved around light and atomic systems. Although these systems provided a large variety of groundbreaking observations, they are limited by the nature of atoms and optical cavities [Wal+06]. Recently, with the fast development of new quantum technologies, the study of light-matter interaction has taken a new perspective. Platforms such as superconducting quantum circuits have shown great potential to study fundamental quantum optics phenomena unattainable by atomic systems. The research in this direction is also motivated by the fast development of quantum computing, where an in depth understanding of fundamental light-matter interactions is of importance to develop reliable qubit control, measurement, and couplings.

Light-matter interactions with couplings of the order of the frequencies of the system are a clear example where superconducting qubits can offer an advantage

over atomic systems. The possibility of engineering each of the elements that form the system allows to design artificial atoms with the desired properties and interactions with arbitrarily large strengths. Although ultrastrong couplings in superconducting quantum circuits have been extensively studied over the past two decades, there is still a long list of experimentally unexplored phenomena, mostly related to the coherence of the system [For+19; Fri+19]. Coherent superconducting quantum systems in the ultrastrong coupling regime are an ongoing quest. The improvement of fabrication techniques and the development of new superconducting materials has opened the door to new and more robust design possibilities. This is the case of superinductors, structures able to provide a large linear inductance without the need for intricate geometric structures such as thin and narrow meandered wires. Systems in the ultrastrong coupling regime, where there is a need for large shared inductances, can greatly benefit from superinductors to reduce design constrains and potentially improve coherence.

The aim of this first chapter is to introduce the basic concepts needed to understand the core topics of this thesis: the ultrastrong coupling regime of light-matter interaction and superinductors. We start in Sec. 1.1 by giving an overview on superconducting qubits with a special focus on flux qubits. We continue in Sec. 1.2 by reviewing the basics of light-matter interaction. This section reveals the convenience of superconducting quantum circuits to study regimes of interaction reaching the ultrastrong coupling regime and how to use them to observe unexplored phenomena. In Sec. 1.3, we introduce the concept of superinductors and their most common implementations. Finally, we conclude the chapter with an overview of the thesis organization putting into context the different topics that will be discussed throughout the text.

1.1 Superconducting qubits

The quantum harmonic oscillator constitutes one of the fundamental systems in quantum mechanics. In the context of superconducting quantum circuits, it can be realized by connecting an inductor together with a capacitor. The resulting potential is harmonic, and the spectrum of the system consists of equally spaced energy levels given by $E_n = \hbar\omega(n + 1/2)$ with ω the resonance frequency of the oscillator. The fact that all transitions are equally spaced makes it very challenging to single out two levels and operate them as a qubit.

Superconducting qubits, instead, rely on anharmonic oscillator potentials built from superconducting circuit elements such as Josephson junctions, capacitors and inductors [Kra+19]. Josephson junction are non-linear inductive elements characterized by the Josephson inductance L_J which can be derived

from the Josephson equations [Jos62] and takes the following form,

$$L_{\mathrm{J}} = \frac{\Phi_0}{2\pi I_{\mathrm{c}} \cos\varphi} = \frac{\Phi_0}{2\pi\sqrt{I_c^2 - I^2}}, \tag{1.1}$$

where Φ_0 is the superconducting flux quantum, I_{c} is the critical current of the junction and φ the phase difference between the wave functions of the two superconductors that constitute the junction. The associated non-linear potential is described by

$$U_{\mathrm{JJ}} = -E_J \cos\varphi, \tag{1.2}$$

where $E_J = \Phi_0 I_C/2\pi$ is the Josephson energy. The addition of the Josephson junction into the well-known harmonic oscillator potential modifies the energy spectrum. The energy difference between the lowest and first excited state will be different from the one between the first and second excited state and, similarly, for the rest of the consecutive transitions. In other words, $\hbar\omega_{0,1} \neq \hbar\omega_{n,n+1}$. Therefore, the anharmonic potential makes the different transitions distinguishable allowing to single out for example, the two lowest states to build a qubit [Rip22].

1.1.1 Types of superconducting qubits

There is a plethora of superconducting qubit types. The choice of circuit elements, their arrangement and their values can define qubits with very different properties, including the resonance frequency, anharmonicity, and resilience to certain types of noise. These properties arise from the difference between intrinsic energy scales of the different circuit elements. These energies consist of the Josephson energy $E_J = \Phi_0 I_{\mathrm{c}}/2\pi$, with I_{c} the critical current of the Josephson junction, the capacitance charging energy $E_C = e^2/2C$, with C the capacitance associated to a capacitor or Josephson junction, and the inductive energy $E_L = \Phi_0^2/(4\pi^2 L)$ with L the inductance associated to an inductor [Kja+20].

Traditionally, qubits have been categorized in two big groups, charge and flux, depending on which is the best well-defined quantum number of the circuit and what elements can modify their eigenstates. Charge qubits can be built connecting a superconducting island to a large reservoir by means of a Josephson junction. The charge is well defined in the island and becomes a good quantum number. Flux qubits, on the other hand, have a well-defined phase. These qubits are built from at least a superconducting loop interrupted by a Josephson junction and an inductor and the resulting eigenstates can be modified by the application of an external flux. Examples of charge qubits include the well-known Cooper-pair box ($E_C \gg E_J$) [Nak+99] and the transmon ($E_J/E_C \sim 30-100$) [Koc+07]. Similarly, examples of established flux qubits are the persistent current qubit

($E_J \gg E_C$) [Orl+99] and the fluxonium qubit ($E_J > E_C$, $E_J \gg E_L$) [Man+09]. In the following section, we provide a more in depth description of flux qubits and their properties.

1.1.2 Flux qubits

There are multiple geometries and approaches to build flux qubits. In general, all flux qubits are built from at least a superconducting loop interrupted by an inductive element and one or more Josephson junctions. In these qubits, the states can be described by circulating currents in the loop and the properties of the system can be modified by threading an external magnetic flux through the superconducting loop.

There is a long list of flux qubits built from different circuit elements and having different ranges of operation. The most well-known examples are the radio-frequency superconducting quantum interference device (rf-SQUID), the C-shunted flux qubit and the fluxonium. Examples of circuit schematics for these types of flux qubits are shown in Fig. 1.1. We start this section presenting the simplest case of a flux qubit consisting of a Josephson junction in parallel with an inductor, the rf-SQUID. The rf-SQUID serves as a preamble for the C-shunted 3-Josephson junction flux qubit which will be of importance to understand the devices presented in Ch. 3 and 4.

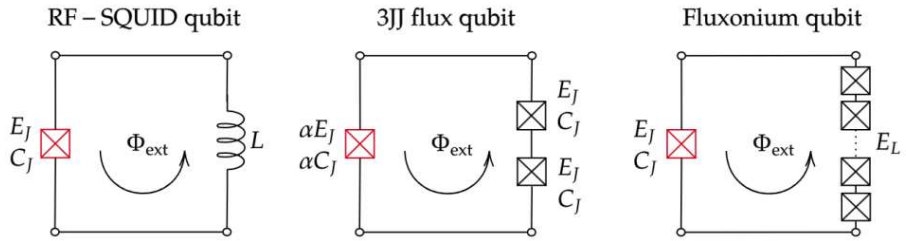

Figure 1.1: Circuit schematics for three different flux qubits: rf-SQUID, 3-Josephson junction flux qubit and fluxonium qubit. Φ_{ext} is the external flux threaded through the loop.

rf-SQUID

Probably one of the simplest anharmonic potentials that can be built from Josephson junctions, capacitors and inductors is the one of the rf-SQUID. The rf-SQUID [Sil+67] consists on a closed superconducting loop interrupted by a

Josephson junction in series with an inductor (see the left panel in Fig. 1.1). The Hamiltonian of this qubit is

$$\hat{\mathcal{H}}_{\text{rf}} = 4E_C\hat{n}^2 + \frac{E_L}{(2\pi)^2}\frac{\hat{\varphi}^2}{2} + E_J\cos(\hat{\varphi} + 2\pi f), \tag{1.3}$$

where E_J and E_C are, respectively, the Josephson and capacitance charging energies of the Josephson junction, E_L is the inductive energy associated to the linear inductor L, and $f = \Phi_{\text{ext}}/\Phi_0$, with Φ_{ext} the external flux applied to the loop.

An intuitive description of the physics of the rf-SQUID can be derived from a simple analysis of its potential energy. The potential consists of a cosine function modulated by a parabolic term. The application of an external flux, f, modifies the overall shape of the potential and, thus, the properties of the system. At zero flux, the minima of the cosine potential aligns with the parabolic term, leading to an effective anharmonic single-well potential. The interesting case comes with the application of an external flux. The flux produces a shift in the cosine term which is maximal for $f = 0.5$. At this flux value, the system has a double-well potential with two equal minima. The lowest two energy states of the system are degenerate and the solutions can be interpreted as a superposition of opposite circulating currents of identical magnitude with wavefunctions localized on each potential well [Rip22]. The system is *frustrated*, thus, there is no favorable current circulation direction in the loop to oppose the external flux $f = 0.5$.

Although the rf-SQUID has a large number of applications as a magnetic flux detector [Cla+06], it presents some challenges when used as a qubit. Since the device contains only one Josephson junction, achieving high reproducibility is difficult. Small deviations in fabrication will significantly impact E_J and, thus, the spectrum of the qubit. On the other hand, the rf-SQUID requires a large loop inductance which implies either using large qubit loops, making the system more sensitive to flux noise [Bra+20], or including materials with high kinetic inductance in the fabrication process [Pel+18].

3-Josephson junction flux qubit

The 3-Josephson junction (3JJ) flux qubit presents a compact design and provides more versatility than the rf-SQUID. The first version of the 3JJ flux qubit was introduced by *Orlando et al.* in 1999 under the name of *persistent-current qubit* [Orl+99] and the first experimental demonstration of the device was carried out by *van der Wal et al.* in year 2000 [Van+00]. The circuit of this qubit consists of a loop interrupted by three Josephson junctions where one of them is made a factor α smaller (see the central panel in Fig. 1.1). The loop inductance is assumed to be small compared with the inductance from the Josephson junctions

and it is neglected during the circuit Hamiltonian derivation. The Hamiltonian of the qubit is

$$\begin{aligned}\hat{\mathcal{H}}_{3\mathrm{JJ}} = 4E_C \left(\frac{1+\alpha}{1+2\alpha}(\hat{n}_1^2 + \hat{n}_2^2) + \frac{2\alpha}{1+2\alpha}\hat{n}_1\hat{n}_2 \right) + \\ - E_J \left(\cos\hat{\varphi}_1 + \cos\hat{\varphi}_2 + \alpha\cos\left(\hat{\varphi}_1 + \hat{\varphi}_2 + 2\pi f\right)\right)\end{aligned} \tag{1.4}$$

where, E_J and E_C are, respectively, the Josephson and capacitance charging energies of the big junctions, α denotes the area ratio between small and big junctions, $f = \Phi_{\mathrm{ext}}/\Phi_0$ with Φ_{ext} the external flux applied to the loop, $\hat{n}_i$ is the charge number operator and $\hat{\varphi}_i$ the phase operator associated to the $i-$th junction.

Depending on the value of α, the 3JJ flux qubit can have very different energy potential landscapes and properties. For values of $\alpha < 0.5$, the potential energy has a single well and the system is said to be in the *plasmon* regime. In this regime, the qubit displays weak anharmonicity and weak flux dispersion. When $\alpha = 0.5$ the system is in the *quarton* regime. For this particular value, the potential can be approximated by a quartic potential ($\sim \hat{\varphi}^4$). The qubit can maintain large anharmonicity ($\sim 1\,\mathrm{GHz}$) and high coherence while keeping a reasonable operating frequency ($\sim 4\,\mathrm{GHz}$). Qubits in the *quarton* regime have also been used as couplers for qubit readout applications[Ye+21; Ye+24]. Finally, the *fluxon* regime arises for $0.5 < \alpha < 1$. In this regime, the potential energy consists of a double-well potential and the qubit is characterized by a strong anharmonicity. [Yan+20]. In Fig. 1.2, we provide three examples of potentials in the *plasmon*, *quarton* and *fluxon* regime, respectively.

In this thesis, we are interested in the *fluxon* regime ($0.5 < \alpha < 1$). To understand the nature of this qubit and its solutions it is convenient to rewrite the potential term in Eq. (1.4) in terms of the sum and difference of phases across the junctions, $\hat{\varphi}_\pm = (\hat{\varphi}_1 \pm \hat{\varphi}_2)/2$, and perform a similar potential study to that given for the rf-SQUID. The potential term of the Hamiltonian under this transformation reads,

$$U_{3\mathrm{JJ}}(\hat{\varphi}_+, \hat{\varphi}_-) = -E_J \left(2\cos\left(\hat{\varphi}_+\right)\cos\left(\hat{\varphi}_-\right) - \alpha\cos\left(2\hat{\varphi}_+ + 2\pi f\right)\right). \tag{1.5}$$

The first term $2\cos\left(\hat{\varphi}_+\right)\cos\left(\hat{\varphi}_-\right)$ has minima at $\hat{\varphi}_\pm = 0$ which can be modified by the second term $\alpha\cos\left(2\hat{\varphi}_+ + 2\pi f\right)$ by applying an external magnetic flux. Similarly to the rf-SQUID case, for $f = 0.5$ the total potential has a double well (see Fig. 1.2 for $\alpha = 0.9$) and the system is frustrated. The qubit will have two stable degenerate states corresponding to each minima of the potential with opposite sign for the phase ($\hat{\varphi}_1 = \hat{\varphi}_2 = \pm\hat{\varphi}^*$), or, similarly, opposite sign circulating currents in the loop [Rip22; Paa09].

3JJ flux qubits are characterized in terms of the qubit gap Δ_{q} and the per-

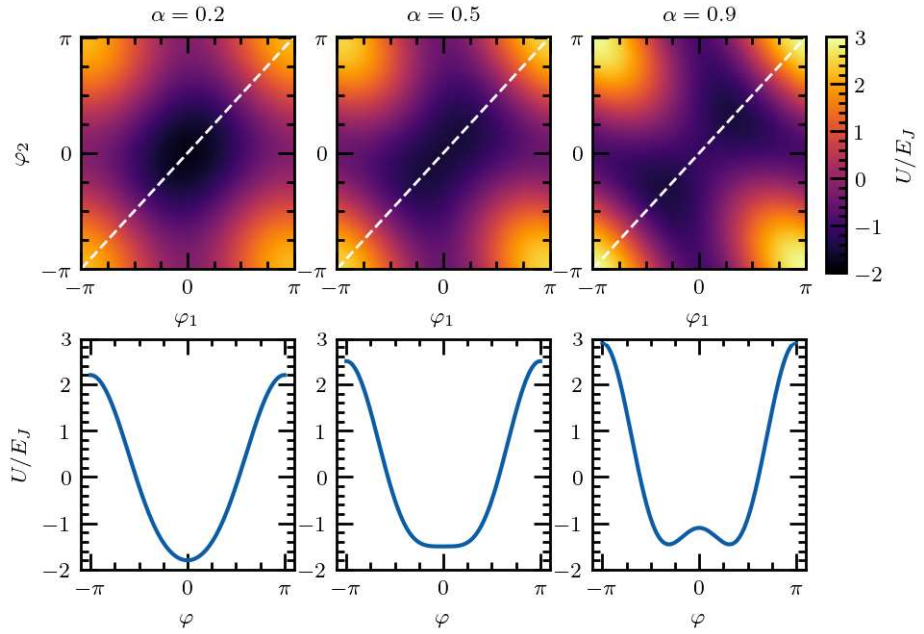

Figure 1.2: Normalized potential (U/E_J) for a 3-Josephson junction flux qubit for three different values of α obtained at the sweetspot $f = 0.5$. The white dashed line indicates the cut $\varphi = \varphi_1 = \varphi_2$ used to obtain the potential profile depicted in the bottom panels.

sistent current I_p. Δ_q represents the qubit energy difference at the sweetspot ($f = 0.5$), while the persistent current gives the magnitude of the circulating current in the qubit ring and can be estimated with $\pm\frac{1}{\Phi_0}\frac{\partial E}{\partial f}$. The expression takes the positive sign for $f > 0.5$ and negative for $f < 0.5$. Since the 3JJ flux qubit can be interpreted in terms of circulating currents, we can also define the associated qubit magnetic dipole moment $\mu = 2I_p$ which will have two preferred directions perpendicular to the qubit plane given by the current direction [Pla07; Rip22].

In general, flux qubits have a high anharmonicity and it is then possible to approximate the system and just keep the two lowest eigenstates. The resulting effective two-level Hamiltonian can be represented in the persistent current basis $\{|L\rangle, |R\rangle\}$,

$$\hat{\mathcal{H}}_{qb} = -\frac{1}{2}\hat{\sigma}_z\epsilon + \frac{1}{2}\Delta_\mathrm{q}\hat{\sigma}_x, \tag{1.6}$$

where $\epsilon = 2I_{\rm p}(\Phi_{\rm ext} - \Phi_0/2)$ is the magnetic energy of the qubit. Using these parameters, the frequency of the qubit at an arbitrary external flux point is given by $\hbar\omega_q = \sqrt{\Delta_{\rm q}^2 + \epsilon^2}$. This expression will become particularly useful when describing the qubit-resonator interaction in Ch. 3.

The original design for a 3JJ flux qubit suffers from low coherence and poor reproducibility [Yos+06; Cha+22]. Asymmetries in the Josephson junctions derived from the fabrication process have a significant impact on the final properties of the qubit and have been known to be one of the major sources of decoherence [Bur+05]. A demonstrated method to improve the design is to include a capacitor shunting the small junction, similar to the approach used in transmons to improve their coherence times. Even though the shunting capacitance decreases the anharmonicity of the qubit, it provides a larger effective capacitance for the small junction and improves reproducibility [Yan+16; Cór+11; Ste+10]. The qubit potential is essentially the same as the one presented in Eq. (1.4) with the change $\alpha \to \alpha + \frac{C_{\rm sh}}{C_J}$ in the kinetic term.

1.2 Light-matter interaction in superconducting quantum circuits

Circuit Quantum Electrodynamics (circuit QED) studies the interaction of quantized electromagnetic fields with superconducting qubits and other circuit elements such as resonators [Bla+21]. The field was born as an analogy to Cavity QED, which considers the interaction of atoms with electromagnetic field modes confined in high reflective optical cavities [Wal+06]. In circuit QED, superconducting qubits play the role of artificial atoms, and resonators provide the tool to confine an electromagnetic mode. Originally, cQED considered fields in the microwave frequency range, but this can be extended both to low, kHz, frequency cavities as well as THz systems. Superconducting quantum circuits have evolved tremendously since the first experimental observation of coherent oscillations with a superconducting qubit [Nak+99]. Nowadays, new types of qubits, improved fabrication, control and understanding of the system have opened the door to the study quantum optics phenomena in a novel range of parameters unattainable by cavity QED systems. In this section, we provide the basic tools to understand light-matter interaction in superconducting quantum circuits, and we give an overview of the different regimes of interaction that can be explored with such a platform.

1.2.1 The Quantum Rabi Model

The description of the simplest form of light-matter interaction in a quantum system has been known for almost a century. Back in 1936, Isidor I. Rabi proposed a model, which nowadays carries his name, to describe the dipolar interaction of a two-level atom with a classical electromagnetic field [Rab36]. The semi-classical description was able to predict phenomena such as Rabi oscillations and light-shifts, but it failed to describe quantitatively processes such as spontaneous emission [Scu+97; Gry+10]. The fully quantized version of the Rabi model was not introduced until 27 years later by the work of E. T. Jaynes and F. W. Cummings [Jay+63]. The nowadays called Quantum Rabi model introduces the quantized version of the electromagnetic field and its physics is given by the Hamiltonian

$$\hat{\mathcal{H}}_{\mathrm{QRM}} = \hbar\frac{\Omega_q}{2}\hat{\sigma}_z + \hbar\omega_r\hat{a}^\dagger\hat{a} + \hbar g\hat{\sigma}_x(\hat{a} + \hat{a}^\dagger), \tag{1.7}$$

where Ω_q and ω_r are the bare two-level system and electromagnetic field frequencies, respectively, g is the coupling coefficient, $\hat{\sigma}_i$ are the Pauli matrices describing the two-level atom and $\hat{a}^\dagger$, $\hat{a}$ are the creation and annihilation operators associated with the electromagnetic field mode. Although it may appear a simple Hamiltonian, many theoretical studies have made efforts into studying the integrability and solvability of Eq. (1.7). It was not until 2011 that D. Braak proposed an analytical solution to the spectrum of the QRM [Bra11]. Still, the analytical expression is fairly complex and the physics of the model are difficult to grasp from its form.

The QRM has traditionally been used to describe the interaction of single atoms interacting with optical cavities. In these systems, the coupling g is much smaller than the atom's and cavity's bare frequencies, thus satisfying the condition $g \ll \Omega_q, \omega_r$. In this regime of interaction, one can apply the so-called rotating wave approximation (RWA), which consists of neglecting the counter-rotating terms $\hat{a}^\dagger\hat{\sigma}_+$ and $\hat{a}\hat{\sigma}_-$, where $\hat{\sigma}_\pm = (\hat{\sigma}_x \pm i\hat{\sigma}_y)/2$ are the atomic raising and lowering operators [Rip22; For+19]. The remaining interaction terms $(\hat{\sigma}_-\hat{a}^\dagger + \hat{\sigma}_+\hat{a})$ describe the interaction in terms of absorption and emission of photons. The resulting Hamiltonian after the elimination of the counter-rotating terms is the so-called Jaynes-Cummings (JC) Hamiltonian [Jay+63],

$$\hat{\mathcal{H}}_{\mathrm{JC}} = \hbar\frac{\Omega_q}{2}\hat{\sigma}_z + \hbar\omega_r\hat{a}^\dagger\hat{a} + \hbar g(\hat{\sigma}_+\hat{a} + \hat{\sigma}_-\hat{a}^\dagger). \tag{1.8}$$

Contrary to the QRM, the JC model is relatively simple, conserves the number of excitations, and can be solved analytically in a convenient form. The eigenstates of Eq. (1.8) can be described in terms of the bare qubit ($|g\rangle$ $|e\rangle$) and resonator ($|n\rangle$) states $\{|e, n\rangle, |g, n+1\rangle\}$, and the energies have an analytical form [Gry+10].

The JC model represents the workhorse in applications of superconducting qubits dealing with qubit-resonator interactions. A well-known example is quantum computing.

The assumption that the coupling coefficient is significantly smaller than the bare frequencies of the system is not necessarily true for all systems described by the Quantum Rabi model. In platforms were the two-level atom and the cavity properties can be fully engineered, one can reach regimes were g is comparable to the frequencies of the system, invalidating the RWA. In this limit, the system enters the so-called ultrastrong (USC) coupling regime and the complete treatment of the Quantum Rabi model is needed to provide accurate predictions of the eigenstates, eigenvalues and dynamical response of the system. As we will see later in this section, superconducting quantum circuits are a clear example of a platform where couplings can be engineered beyond the Jaynes-Cummings Hamiltonian limit.

1.2.2 Ultrastrong coupling regime of light-matter interaction

In the previous section, we have seen that when the coupling coefficient approaches the bare frequencies of the system, the counter rotating terms $\sim (\hat{a}\hat{\sigma}_- + \hat{a}^\dagger\hat{\sigma}_+)$ become sizeable and cannot be neglected. This limit defines the USC regime and extends for couplings $0.1 < g/\omega_r < 1$. Beyond $g/\omega_r > 1$, the system enters a different regime with distinctive features known as the deep strong coupling regime (DSC). The physics in the USC regime gradually changes for increasing couplings. In fact, two distinctive sub-regimes can be identified depending on how the counter-rotating terms are treated and what approximate Hamiltonians can be used [Ros+17b]. They are the perturbative and the non-perturbative USC regimes.

The perturbative USC regime comprises couplings between $0.1 < g/\omega_r \lesssim 0.3$. In this range of interactions, one can consider a perturbative expansion of the counter-rotating terms as an off-resonant field. The physics in the non-perturbative USC regime is well described by the so-called Bloch-Siegert (BS) Hamiltonian [Bea+11; For+10],

$$\begin{aligned}\hat{\mathcal{H}}_{BS} = \hbar\frac{\Omega_q}{2}\hat{\sigma}_z + \hbar\omega_r\left(\hat{N}+\frac{1}{2}\right) + \hbar\omega_{BS}\left(\hat{\sigma}_z\left(\hat{N}+\frac{1}{2}\right)-\frac{1}{2}\right) + \\ + \hbar(g(\hat{N})\hat{a}^\dagger\hat{\sigma}_- + \hat{a}\hat{\sigma}_+ g(\hat{N}))\end{aligned} \tag{1.9}$$

where $\hat{N} = \hat{a}^\dagger\hat{a}$ is the harmonic oscillator number operator, $\omega_{BS} \equiv g^2/(\omega_r + \Omega_q)$ is the Bloch-Siegert shift and $g(\hat{N}) \equiv -g(1 - \hat{N}\omega_{BS}/(\omega_r + \Omega_q))$ is the renormalized coupling constant [Blo+40]. The BS shift quantifies the magnitude of

the perturbative effect of the counter-rotating terms on the system spectra. In fact, these terms produce a repulsion between the atomic and harmonic oscillator levels defined by the JC model. In particular, the oscillator (atomic) transition is shifted a magnitude ω_{BS} downwards (upwards) in frequency.

As the coupling increases to the regime $0.3 < g/\omega_r < 1.0$, the perturbative treatment of the counter-rotating terms fails and the system enters the so-called non-perturbative USC regime. The two-level atom and the electromagnetic field mode become highly hybridized, and one needs to treat the complete QRM (Eq. (1.7)) for arbitrary couplings, where new physics arises. A direct consequence of the presence of the counter-rotating terms is the breaking of the conservation of excitation number. This opens the possibility to absorb/emit multiple photons at the same time in a coherent and reversible manner [Gar+16]. Another consequence is the possibility to have transitions between dressed states containing contributions from various numbers of photons and atomic excitations. This gives rise to possibly one of the most striking particularities of the non-perturbative USC regime, which is the squeezed ground state with a finite number of photons. These photons are sometimes referred as virtual photons because they cannot be directly detected. There are proposals to extract and detect this photons that include using lower uncoupled levels [Gia+24; Fal+19], ancillary qubits [Lol+15], or a fast modulation of the interaction strength [De +09].

In order to illustrate the spectral differences between the coupling regimes presented in this section, Fig. 1.3 provides the spectrum of a qubit-resonator system calculated with the QRM and the JC model for different interaction strengths (see Sec. 1.2.3 for more details on qubit-resonator couplings). As the coupling increases, the differences between models become more pronounced. We observe an increasing shift between JC and QRM in the resonator transition, a direct consequence of the effect of counter-rotating terms. For couplings in the non-perturbative USC regime (third panel), the difference between models becomes significant even outside the qubit sweetspot ($\Phi_{\text{ext}} = 0.5\Phi_0$).

For completeness, let us consider the case of coupling coefficients beyond $g/\omega_r > 1.0$. Under these circumstances, the interaction becomes the dominant energy scale of the system and a new regime of interaction, the DSC regime, arises. One of the main characteristics of this regime is the collapse and revival of the initial population [Cas+10]. The approximate Hamiltonians and physics of the DSC system differ from the USC and require a specific treatment which is beyond the scope of this thesis.

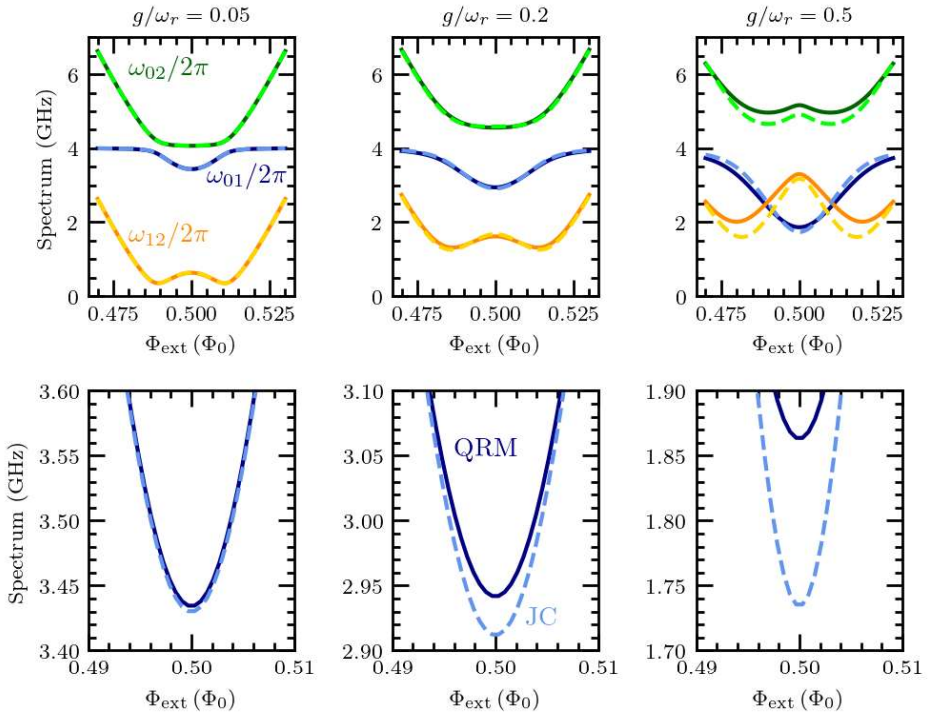

Figure 1.3: Qubit-resonator spectra calculated using the QRM (solid) and JC (dashed) for different couplings g. The parameters used for the simulation are $\Delta_{\rm q}/h = 3.5\,\text{GHz}$, $I_{\rm p} = 30\,\text{nA}$ and $\omega_r/2\pi = 4\,\text{GHz}$. The upper panels show the transitions corresponding to the first two energy levels of the system, while the lower panels are a zoom near the sweetspot for ω_{01}.

1.2.3 Ultrastrong coupling regime with superconducting qubits

In circuit QED, qubits play the role of artificial atoms while resonators provide the tool to confine an electromagnetic mode. There are numerous ways of coupling qubits to resonators. The arrangement and circuit elements used to couple them will depend on the strength of the interaction required, the application and the type of qubit used. For example, ultrastrong inductive couplings will be more suited for flux qubits since their eigenstates correspond to well-defined persistent current states, while ultrastrong capacitive couplings will be more suited for charge-based qubits. In both instances, the description of the interaction is of a

dipolar type and can be rewritten in a similar form to the QRM (see Ch. 3 for an example of a flux qubit-resonator coupling).

Inductors are the preferred choice to study USC in flux qubit-resonator systems. Several approaches can be followed to couple both circuits. Figure 1.4 depicts different inductive coupling strategies: (a) by sharing a Josephson junction, (b) by placing the two circuit elements close to each other (mutual geometric inductance) or (c) by sharing a linear inductor. In the following sections we describe each in more detail and we give some insights on how to achieve the USC regime with each of them.

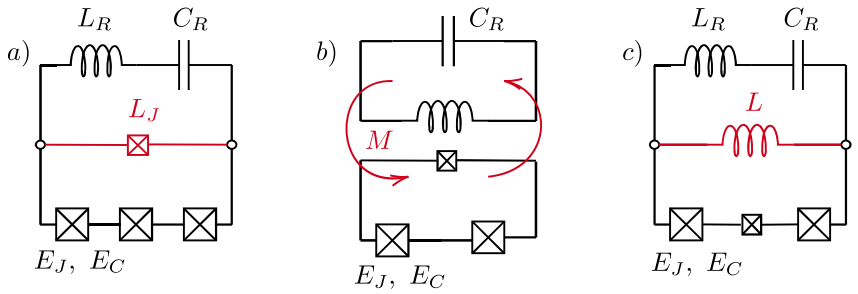

Figure 1.4: Different flux qubit-resonator inductive couplings. (a) Sharing one of the qubit Josephson junctions, (b) mutual geometric inductance and (c) sharing a linear inductor.

Shared Josephson junction

The natural choice to boost the qubit-resonator coupling is to use a shared circuit element, such as a Josephson junction, that can provide a large inductance L_J. There are namely two approaches. The first one consists of sharing a large Josephson junction in the linear regime. This is a junction with critical current I_c much larger than the current flowing through it. Under this condition, the junction can be approximated as a linear inductor with $L_\mathrm{J} = \Phi_0/2\pi I_\mathrm{c}$, with, the dipolar interaction and the coupling coefficient being directly proportional to L_J [Nie+10]. The second approach depicted in Fig. 1.4 (a) consists of sharing one of the qubit junctions with the resonator circuit. The coupling in this case depends on the magnetic dipole moment of the qubit which can be calculated as the expectation value $\langle 0|\hat{\varphi}|1\rangle$, where $\hat{\varphi}$ is the phase across the shared junction [Per+13]. Although it is straightforward to obtain a large coupling using Josephson junctions, they provide a set of inconveniences. Specifically, they can introduce stray nonlinearities in the coupling and may introduce noise in the form of two-level system defects localized in the insulator of the junction [Bil+17] and

quasiparticle tunneling [Ris+13].

The use of shared Josephson junctions has been the most ubiquitous approach to attain qubit-resonator couplings extending from the USC regime up to the DSC regime. Examples include the work from *T. Niemczyk et al.*, which is one of the first experimental demonstrations of USC using superconducting qubits. In [Nie+10], the qubit shares a large Josephson junction between the qubit loop and a transmission line resonator providing $g/\omega_r \sim 0.12$. More recent works have been able to explore couplings in the non-perturbative USC regime [For+17] and, even the DSC regime [Yos+17b; Yos+17a] using shared qubit junctions or SQUIDs.

Mutual inductance

Consider two superconducting loops placed next to each other (Fig. 1.4). The mutual inductance between the two loops is defined as the magnetic flux through the first loop produced per unit current circulating in the second loop. Equivalently to the classical case, this quantity depends on the geometry and the distance between loops [Cot+91]. In quantum annealing, qubit-qubit and qubit-resonator interactions are often mediated by the mutual inductance between the circuits located in different chips [Ros+17a; Web+17].

The caveat of the mutual inductance approach is that in order to boost the coupling, one requires large qubit loops [For+19]. Furthermore, large qubit loops make the qubit more sensitive to flux noise since the noise scales with the perimeter of the loop [Bra+20], making it very challenging to have coherent qubit-resonator systems. In general, mutual inductive couplings are not considered as a practical approach to reach qubit-resonator couplings in the USC regime [For+19].

Shared linear inductor

The last option depicted in Fig. 1.4 (c) comprises the use of a shared linear inductor between qubit and resonator. For inductances of the order of the resonator and qubit junction inductances, the coupling depends on the magnetic dipole moment of the qubit which can be calculated as the expectation value $\langle 0|\hat{\varphi}|1\rangle$, where $\hat{\varphi}$ is the phase across the shared inductor [Per+13]. This approach offers several advantages. First, the inductor is linear so we can avoid stray non-nonlinearities coming from the shared circuit element. Secondly, we can benefit from superconducting materials showcasing large kinetic inductance to provide a large coupling inductance in a relatively small space. These materials are called superinductors and will be presented in the next section. Even though these materials can have a non-linear component, it can be reduced by adjusting the geometry of the design and film resistivity [Mal+18; Ho +12]. The disadvantage of using large shared linear inductors is that they introduce a harmonic term in the qubit potential.

Depending on the qubit design, this can lead to lower qubit persistent currents, possibly decreasing the coupling strength.

To our knowledge, only two experimental proposals used a shared linear inductor as qubit-resonator coupler reaching the USC regime [For+10; Che+17]. The work from *P. Forn-Díaz et al.* used a shared thin Al wire connecting both circuits and providing an estimated inductance of $L \sim 25\,\mathrm{pH}$, enough to reach $g/\omega_r \sim 0.1$. To circumvent the relatively low shared inductance, they used a qubit with an extremely large persistent current ($\sim 500\,\mathrm{nA}$), with the consequent detrimental effect on qubit coherence. The approach followed by the work from *Z. Chen et al.* is similar to [For+10]. The qubit is designed with a large persistent current $I_p \sim 250\,\mathrm{nA}$ and a sufficiently large loop to have enough inductance to reach a coupling $g/\omega_r \sim 0.1$.

Linear galvanic couplings have been realized beyond the scope of USC regime studies. For example, in the work from *A. Fedorov et al.* [Fed+10], a gradiometric flux qubit is coupled galvanically to a resonator with an Al line. The system reached the strong coupling regime with an estimated coupling of $g/\omega_r \sim 0.05$. More recently, in [Gei+24; Ihs+25], the authors proposed a fluxonium qubit-resonator galvanic coupling based purely on kinetic inductance. Unlike the previous cases, the galvanic coupling is implemented in granular Aluminum, a material displaying a high kinetic inductance.

1.3 Superinductors

In Sec. 1.1 we have introduced different circuit elements typically used in superconducting quantum circuits, namely inductors, capacitors and Josephson junctions. In this section, we will focus on superinductors, a new building block for superconducting qubit technologies used in high-impedance qubits such as the fluxonium [Man+09; Grü+19] and in designs of high-impedance environments [Fra+25; Lég+19; Zap+24]. Superinductors are superconducting elements with impedances (Z) similar or greater than the resistance quantum $R_Q = h/(2e)^2 \simeq 6.5\,\mathrm{k\Omega}$. Besides the large impedance, in order to operate in qubit circuits, superinductors are also required to display low microwave losses self resonances well above the operating frequencies of the device, and small nonlinearities [Man12; Mas+12; Bel+12].

Reaching an impedance above R_Q can be challenging with standard geometric inductance. Increasing the length of a straight wire will come with an increase of self-capacitance. Without considering the effect of the kinetic inductance of a film, the maximum impedance that one can achieve is bound by the vacuum impedance $Z_0 = \sqrt{\mu_0/\epsilon_0} \ll R_Q$, with μ_0 and ϵ_0 the vacuum permeability and permitivity, respectively [Man12]. Instead, by considering more complex geometries, the design of the inductor can benefit from the mutual inductance. In

particular, it has been shown that one can reach $Z > R_Q$ by winding the wire in a spiral shape [Per+20].

The space available to pattern the inductor in some qubit applications is limited, and geometric superinductors may be challenging to implement besides having a higher sensitivity to flux noise due to their length. Therefore, one has to resort to alternative methods to build superinductors. In the following subsections, we briefly discuss two approaches to realize superinductors: arrays of Josephson junctions and disordered superconductors. The former one relies on the large inductance provided by Josephson junctions, while the latter exploits the concept of kinetic inductance.

1.3.1 Josephson junction arrays

Usual Josephson tunnel junctions are built from two superconductors separated by an insulating layer. Given the ease in obtaining and manipulating Al, $Al/AlO_x/Al$ Josephson junctions have become the most widespread materials stack in the superconducting quantum circuit community. The properties of the junction, namely the critical current I_c, can be easily tuned by changing the area or the thickness of the insulating oxide layer. This versatility together with the possibility of achieving inductances of the order of few a nH, while keeping them in a near linear response regime, make Josephson junctions an obvious approach to realize superinductors.

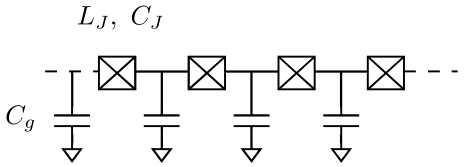

Figure 1.5: Schematics of an array of Josephson junctions. C_J and L_J are the capacitance and inductance associated to a single Josephson junction. C_g indicates the island's capacitance to ground.

By preparing Josephson junction chains with carefully designed junction areas and currents, one can engineer a medium with a large impedance and large inductance $L \simeq NL_J$, where N is the number of Josephson junctions in the chain [Man12]. However, arrays of junctions also introduce a set of inconveniences. First, the system needs to operate in a linear regime, this implies using significantly long chains of junctions with large critical currents to achieve the desired inductance. Also, Josephson junctions have an associated junction capacitance, C_J, and each island has a capacitance to ground, C_g (see Fig. 1.5 for a schematic of an array of junctions). The capacitance and inductance of a junction define

the so-called plasma frequency $\omega_p = 1/\sqrt{L_J C_J}$ which typically takes values in the $\omega_p/2\pi \sim 10 - 40\,\text{GHz}$. The plasma frequency lies above the operating frequencies of superconducting qubit devices, but since the array of junctions has a finite length, it will also have some associated modes with frequencies below ω_p. The frequency of these modes can be pushed towards ω_p by designing a small ratio of C_g/C_J. Overall, designing an array of Josephson junctions operating in a linear regime and suited as a superinductor requires a careful design of C_J, L_J and C_g to avoid parasitic modes and stray nonlinearities [Grü19]. Still, junction arrays achieve the best performance when making qubits so far [Ngu+19; Som+23; Wan+25].

1.3.2 Disordered and granular superconductors

An alternative to Josephson junction arrays are superconducting materials which naturally display large kinetic inductance. In the following subsections, we describe the concept of kinetic inductance and give an overview on disordered and granular superconductors.

Kinetic inductance

To understand the concept of kinetic inductance, we need to introduce three characteristic lengths: the superconducting penetration depth λ, the coherence length ξ and the mean free path l_e. λ represents the distance that a magnetic field penetrates into the superconductor, ξ gives the average distance of electrons forming a Cooper pair and l_e is the average distance traveled by an electron inside the material before a scattering event [Lóp+25; Tin04].

The kinetic inductance of a superconductor is related to the inertia of Cooper pairs and it is defined in terms of the penetration depth [Rot+16],

$$L_k = L_{k,\square} N = \mu_0 \lambda N \tag{1.10}$$

where μ_0 is the magnetic vacuum permeability and N the number of squares of a wire of length l and width w. For thin films where the thickness is much smaller than the penetration depth ($t \ll \lambda$), an external perpendicular magnetic field fully penetrates the sample and a correction to the kinetic inductance has to be considered [Kau78; Lóp+25],

$$L_k \equiv \mu_0 \lambda_{\text{thin}} = \mu_0 \frac{\lambda^2}{t}. \tag{1.11}$$

In disordered and granular superconductors, the impurities modify l_e and,

consequently, ξ [Pip+53]

$$\frac{1}{\xi} = \frac{1}{\xi_0} + \frac{1}{l_e}, \tag{1.12}$$

where ξ_0 is the coherence length of the pure material in the bulk. In the dirty limit ($l_e \ll \xi_0$), the BCS expression for the penetration depth [Tin04] can be approximated by

$$\lambda^2 \simeq \lambda_L(0)^2 \frac{\xi_0}{l_e}, \tag{1.13}$$

where $\lambda_L(0)$ is the London penetration depth in the clean limit at $T = 0\,\mathrm{K}$. Introducing the latter result in Eq. (1.11), and using the BCS definition of $\xi_0 = \hbar v_F/(\pi\Delta(0))$ with v_F the Fermi velocity and $\Delta(0)$ the superconductor gap at $T = 0\,\mathrm{K}$, we obtain an approximation for the kinetic inductance

$$L_\mathrm{k} = \frac{\hbar R_n}{\pi\Delta(0)} = \frac{\hbar R_n}{1.75\pi T_c k_B}, \tag{1.14}$$

where we have employed the concept of normal-state conductivity $\sigma_n = \rho_n^{-1} = (R_n\sigma/l)^{-1}$ [Gle+20]. Equation (1.14) already suggests that a large kinetic inductance will be related to large normal state resistance.

Disordered and granular superconductors

Disordered and granular superconductors generally display large kinetic inductance and their use as a superinductor is widely spread in the superconducting quantum circuit community. Although granular superconductors can be considered disordered from a morphological point of view, the inhomogeneities in these materials are well above the atomic level. These superconductors contain clusters of superconducting metal several nm in size surrounded by a matrix of an insulator or a normal metal. In contrast, in disordered superconductors the disorder is generally considered on the atomic scale [Gan+10; Gle+20].

The most widely used granular superconductor in superconducting qubit circuits is granular Aluminum (grAl). GrAl films are fabricated by evaporating Al in an O_2 atmosphere, the resulting material consisting of Al grains embedded in a matrix of AlO_x. The Al grain size and the AlO_x insulating barriers shape the properties of the material which can differ significantly from Al. In grAl, the resistivity of the film is given by the inter-grain coupling and can be tuned by changing metal deposition parameters such as the evaporation rate, the O_2 concentration or the substrate temperature. One of the well-known properties of grAl is its enhanced critical temperature first reported in the 60s by *Abeles et al.* [Abe+66]. The critical temperature of grAl can be as high as a factor three of the critical temperature of bulk Al. Nowadays, fabrication techniques under cooled

substrates have achieved grAl samples with grain sizes $\sim 2\,\mathrm{nm}$ and critical temperatures above $3\,\mathrm{K}$ [Deu+73a; Des+25]. Yet, probably one of the most striking properties of grAl is its phase diagram, where T_c can be modified with O_2 doping and displays a dome-shape distribution as a function of room-temperature resistivity [Deu+73b; Deu+73a].

On the other hand, materials such as NbN, TiN, or NbTiN are often regarded as highly disordered films with disorder at the atomic scale. The disorder in these type of superconductors can be controlled by changing deposition parameters such as the stoichiometry. The increasing disorder is translated in an increase of normal state resistivity. In contrast to grAl, the critical temperature in atomically disordered superconductors does not display a dome shape. Instead, it decreases with increasing resistivity and disorder until superconductivity is quenched [Gle+20]. In fact, the superconductor-to-insulator transition (SIT) in highly disordered superconductors is generally of an Anderson type (growing disorder in a system of non-interacting electrons). In contrast, for grAl the SIT is of Mott-type, which considers a decreasing electron concentration in the presence of Coulomb electron interactions [Gan+10; Bac+15].

Table 1.1 summarizes $L_{\mathrm{k},\square}$ for different superconducting materials measured in the context of superconducting quantum circuits. In general, grAl films have a wider range of L_k tunability than other nitride-based superconductors.

Table 1.1: Summary of kinetic inductance per square ($L_{k,\square}$) in different disordered and granular superconductors measured in the context of superconducting quantum circuits.

Material	Reference	$L_{\mathrm{k},\square}$ (nH /□)	Structure	Type
grAl	[Grü+18]	2.0	Stripline resonator	Granular
	[Gup+25]	0.05 - 0.32	Resonator	Granular
	[Zha+19]	1.2 - 2.0	Resonator	Granular
	[Grü+19]	0.1	Fluxonium	Granular
NbN_x	[Nie+19]	0.082	Nanowire	Disordered
	[Fra+23]	0.035 - 0.173	Resonator	Disordered
NbTiN	[Sam+16]	0.035 - 0.075	Nanowire resonator	Disordered
	[Bre+22]	0.23-0.40	Transmission line resonator	Disordered
TiN	[Ami+22]	0.001 - 0.239	Resonator	Disordered
	[She+18]	0.001 - 0.234	Thin film / Resonator	Disordered
NitrAl	[Tor+24]	0.001 - 0.422	Thin film	To be studied
	[Lee+24]	0.001 - 0.350	Thin film	To be studied

1.3.3 Superinductors for superconducting quantum circuit applications

In the following, we provide a brief overview of some of the most common uses of superinductors.

Superinductors have been extensively used in the superconducting qubit community. In terms of qubit applications, the fluxonium has probably benefited the most from them. Fluxonium qubits require loop inductances of the order of tens or hundreds of nH. The first experimental demonstration used an array of Josephson junctions [Man+09], however, nowadays it is common to see implementations of fluxoniums with grAl [Grü+19; Rie+23] and other nitride-based disordered superconductors [Haz+19]. Although there are proposals that use superinductors in other types of qubits such as transmons [Win+20], rf-SQUIDs [Pel+18], or other flux qubit types [Gei+24], the applications of these materials go beyond the qubit itself. Resonators fabricated in materials displaying low losses, high critical temperatures, and high resilience to magnetic fields are of key importance for quantum computing and quantum information processing applications. Some disordered nitride-based superconductors like NbTiN and TiN fulfill these requirements, especially when they are far from the SIT [Mül+22; Vis+10; She+18].

Sensing applications have long benefited from high kinetic inductance materials. It is the case for example of kinetic inductance detectors. These systems are based on the change in the imaginary part of the impedance in a resonator produced by the absorption of radiation and the subsequent generation of quasiparticle excitations. Materials such as TiN or NbTiN have traditionally been used to build these type of detectors [Bas12] but there are also proposals with grAl and other superinductors [Val+19].

Superinductors have also enabled novel quantum optics studies in circuit QED. Using Josephson junction chains, one can build high impedance environments. This approach recently allowed the detection of multi-mode fluorescence in a small Josephson junction embedded in a SQUID transmission line [Fra+25; Fra23].

Finally, superinductors can lead to new possibilities to study ultrastrong light-matter couplings. As we will see in Chs. 3 and 4, superinductors can be used to implement flux qubit-resonator couplings well into the non-perturbative USC regime. One of the advantages of this approach is that qubit persistent currents can be kept relatively low, implying larger coherence times, while having access to large shared inductances, and thus, large couplings.

1.4 Thesis overview

The main focus of this thesis is the study of ultrastrong flux qubit-resonator couplings enabled by superinductor materials. We provide two novel studies that define the structure of the thesis: the experimental implementation of a flux qubit galvanically coupled to an LC resonator in the USC regime using grAl as a coupler; and the study of the superconducting properties of Nitridized Aluminum thin films as a potentially new superinductor.

Before entering into the details of the studies mentioned above, we devote a substantial part of Ch. 2 to present the recipes for superconducting qubit fabrication. This thesis is the first in the group to include fabrication in-house of qubits, and many of the procedures have been developed from the ground up. We describe in detail the calibration of Josephson junctions and grAl fabrication. Additionally, we provide the multi-step qubit fabrication procedure developed to include grAl as part of the qubit loop. We conclude the chapter with an overview of the setup and the basic qubit measurement techniques used in Ch. 4.

Chapter 3 is the first devoted to the study of a flux qubit galvanically coupled to a resonator in the USC regime. The chapter presents the basic theory, circuits and Hamiltonians used in Ch. 4 to design the qubit-resontator system. We start from the basic elements: the 3-Josephson junction flux qubit with a non-negligible inductance and build up to the complete flux qubit-resonator system. Along with the different Hamiltonian derivations, we provide the expressions of the coupling coefficient in terms of the circuit elements and different numerical approaches to simulate the qubit-resonator system.

Chapter 4 uses the theoretical tools derived in Ch. 3 to design, implement and measure a flux qubit-resonator system in the USC regime. The design has two main particularities: it uses grAl as a flux qubit-resonator coupler, and it contains two feedlines to probe the qubit and the resonator independently. Besides the previous elements, important efforts are set towards the design of a coherent system in the USC regime. This chapter also includes the first implementation and measurements of a flux qubit coupled galvanically by a superinductor to an LC resonator in the USC regime. We show that even with the low persistent current of the qubit, the coupling is able to reach $g/\omega_r \simeq 0.13$. We conclude the work in superinductor-based USC studies with an outlook on future devices and measurements.

Finally, in Ch. 5 we study the superconducting properties of Nitridized Aluminum (NitrAl) thin films, a novel superinductor material developed in IFAE. This part of the thesis provides an extensive characterization of the critical temperatures, temperature-resistance behavior and critical magnetic fields for a set of 100 nm NitrAl films sputtered in different N_2 flows. We observe enhanced critical temperatures compared to those of Al and a similar dome-shape distribution

of T_c as a function of resistivity compared to grAl. We conclude the chapter with a first set of resonators patterned in this novel superconductor with insights on future studies involving NitrAl films.

The last chapter of the thesis, Ch. 6, reviews the main conclusions of the different studies and provides an outlook into future experiments.

Chapter 2

Experimental methods

Contents

2.1 Micro and nanofabrication 41
2.1.1 Microfabrication techniques and recipes 42
2.1.2 Granular aluminum fabrication 45
2.1.3 Qubit and junction fabrication 48
2.2 Experimental setup 58
2.2.1 Room temperature characterization setup 58
2.2.2 Qubit and DC measurement setup 58

In this chapter, we describe the different fabrication methods used in this thesis to produce flux qubit devices, as well as the different room-temperature and low-temperature setups used to carry out the measurements described in the rest of this thesis. Especial attention is given to the fabrication of granular Aluminum (grAl) and the multi-layer flux qubit fabrication recipe developed for the devices presented in Ch. 4.

2.1 Micro and nanofabrication

The devices presented in this thesis are fabricated in different cleanroom facilities available in Barcelona. The optical lithography is performed at the Institute of Photonic Sciences (ICFO) and the Centro Nacional de Microelectrónica (CNM), the electron beam lithography (EBL) is carried out at CNM and the Catalan Institute of Nanoscience and Nanotechnology (ICN2), and, finally, the evaporations and lift-offs are performed at the Institute of High Energy Physics (IFAE) cleanroom.

The fabrication of qubit devices presented in Ch. 4, and depicted in Fig. 2.1, involves a total of five fabrication steps:

1. Alignment markers

2. Resonators and ground planes
3. Granular Aluminum
4. Josephson junctions
5. Contacts between different layers

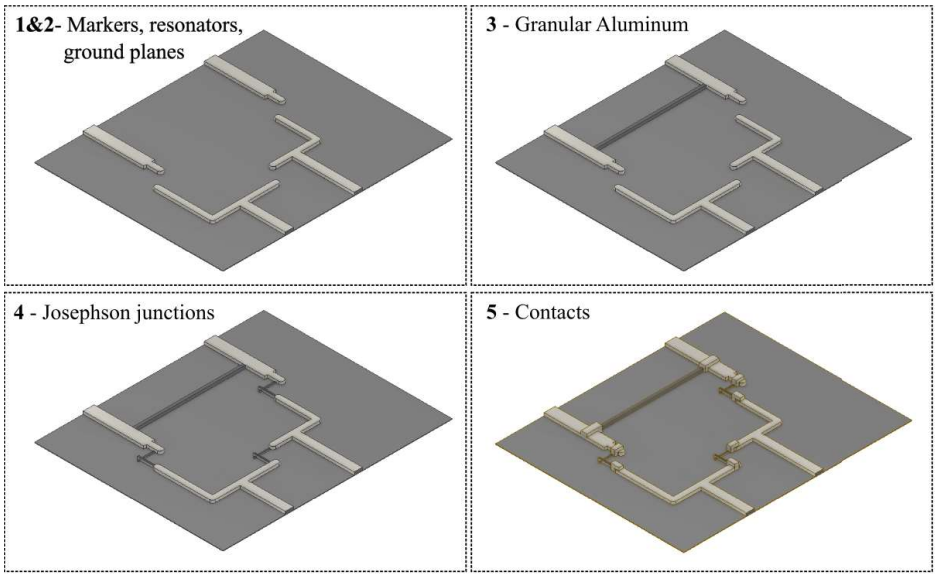

Figure 2.1: Schematics of the qubit loop showing the different fabrication steps. The lighter gray areas represent the Al structures connecting to the resonator, while the darker structures in steps 3-5 show the grAl and Josephson junctions.

Most of the fabrication recipes presented in this chapter had to be developed during the course of this thesis. In the next sections, we present the recipe development for micro- and nanofabrication of superconducting qubit devices with special attention to Josephson junctions and grAl. The detailed fabrication of qubit devices used in this thesis is given in Appendix A.

2.1.1 Microfabrication techniques and recipes

We begin this chapter by the microfabrication. The superconducting qubit devices used throughout the thesis generally require, besides the qubit, large ground planes, feedlines and planar resonators. These structures have dimensions that

can reach up to hundreds of microns and they are suited for optical lithography. The pattern takes between seconds up to few minutes and the resolution can be as good as $\sim 1\,\mu$m depending on the instrument and resist used.

In the following sections, we will assume to start with a substrate which has been previously cleaned in acetone and isopropanol. If the previous fabrication step required the use of resists, we include a plasma descumming step into the cleaning. The full set of fabrication can be found in Appendix A.

Markers

Chips involving more than one fabrication step require alignment markers. Alignment markers are structures designed at the micron scale that help align the different layers of the fabrication process with respect to each other. The choice of shape and material depends mostly on the type of lithography and instruments used throughout the process. In our case, we have access to a Karl SUSS microtech mask aligner, a Heidelberg maskless aligner, and two different 30 kV Raith EBL systems.

Generally, one needs markers of several hundreds of microns in length and tens of microns in width to operate the mask aligner on a chip that already contains a pattern. The requirements are more flexible in the case of the maskless aligner. Squares of few microns in width placed at the corners of the chip are enough to perform a good alignment. Finally, the different Raith EBL units need local markers at the different locations where we want to pattern structures, i.e., they need to fit inside an EBL write-field. The different requirements from each instrument must be taken into account at the time of designing a mask with markers.

The alignment accuracy is different for each system and can be affected by the real dimensions of the markers and the presence of a small vertical tilt in the sample. In general, the Raith EBL units can align with accuracies of few nm while for the optical lithography systems the deviations are in the range 100 nm − 500 nm. Qubit designs should be flexible enough to accommodate misalignments between layers.

Markers are fabricated on a 4″ wafer-scale using a Karl Suss mask aligner and a stack of LOR3A+HPIR6512 positive photoresist (see Sec. A.2.1 for the detailed recipe). Fig. 2.2 shows a mask design together with different zoom-in images from chips, devices and markers present on the mask. Each device contains "L"-shaped markers accompanied by a circular shape to perform alignment in optical lithography processes. The smaller blocks of four "L"-shaped markers are intended for EBL. The spacing between markers is 90 µm to fit inside a 100 µm write-field. Several device copies also contain blocks of four "L"-shaped markers spaced 190 µm in case bigger write-fields are used.

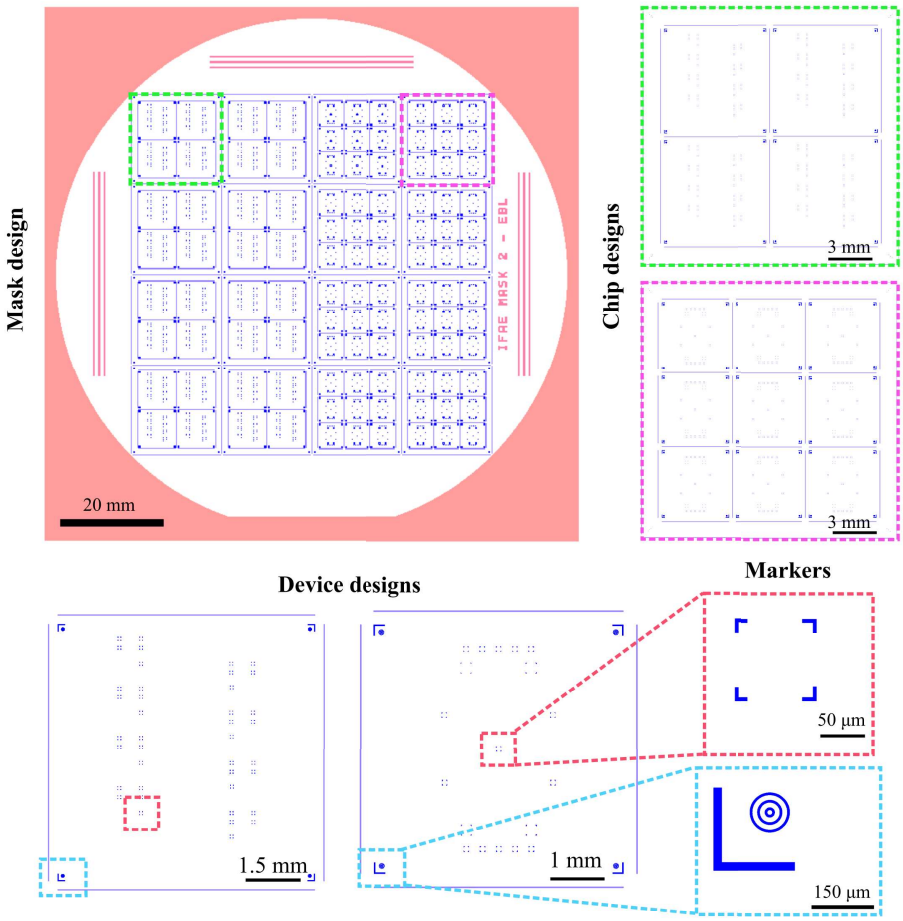

Figure 2.2: Mask design for Pd markers. The mask design contains an array of 16 chips of 2 cm × 2 cm with two different device designs. The device depicted on the left has dimensions 7.5 mm × 7.5 mm and the one on the right is 5 mm × 5 mm. On each device we have mainly two types of markers, four concentric "L"-shaped EBL markers spaced 90 µm and a combination of "L"-shaped and circular markers for optical lithography.

We choose Pd as the material for our markers. The choice of Pd is motivated by the fact that it displays good contrast in the EBL systems and it is chemically compatible with Al. To ensure a good contact with the Si substrate, we first

evaporate a layer of 3 nm of Ti followed by 30 nm of Pd. We use a standard lift-off process consisting in N-methyl-2-pyrrolidone (NMP) at 75 °C for approximately 2 h. Once the residual metal has come off, we clean the wafer in isopropanol and we blow-dry the surface with N_2 gas.

Ground plane, resonators and feedlines

The process followed to fabricate resonators, ground planes and feedlines is similar to the one used for markers. The choice of resist type and instrument will depend on the design and metal deposition technique. Generally, for metal evaporation and designs which are densely metalized, we use a negative photoresists. This is the case of the devices presented in Ch. 4. For designs where only small portions of the device need to be metalized it will be more appropriate to use positive photoresists, which is the case for markers and DC test structures such as the ones presented in Section 2.1.2. In general, we can achieve better resolution with the maskless aligner, reaching down to 1 µm. The detailed photolithography recipes are described in Section A.2.

2.1.2 Granular aluminum fabrication

GrAl can be obtained by evaporating Al in an oxygen atmosphere. Depending on the partial pressure of oxygen and the evaporation rate, the resulting material will display different resistivity, critical temperature, and grain size [Grü19; Lev+19; Bac+14]. The advantage of grAl over other disordered or granular superconductors is the relatively simple fabrication process and compatibility with Al-based Josephson junction fabrication. However, a drawback of grAl is the lack of reproducibility. Small changes in the evaporation rate, in the oxidation, or even the oxygen contamination of the Al source, can affect the properties of the material [Rot+16; Jan+25].

At IFAE, we use an Al-dedicated Plassys electron beam evaporator. This evaporation system has two separate chambers that hold vacuum independently. The top one (load-lock) is smaller and is used to load samples, perform Argon milling, and O_2 microwave plasma descumming. The pressures in this chamber are typically in the 1×10^{-7} mbar range. The bottom chamber (process chamber) contains the different metal targets and holds the lowest pressures ($\sim 2.5 \times 10^{-8}$ mbar). The evaporator has the possibility of incorporating high purity Ar, N_r and O_2 through different valves and mass flow controllers connected to the load-lock. In this section, we will focus on the incorporation of O_2 during metal deposition.

The grAl fabrication process used in this thesis is similar to the one reported previously in the literature [Gei+24; Grü19] and follows these steps:

- Pump down the load-lock chamber for approximately 2.5 h, or until the pressure is around 2.6×10^{-7} mbar. The pressure in the process chamber should lie below 5×10^{-8} mbar.
- Perform and initial Ti evaporation to decrease further the background pressure. During the Ti evaporation, the substrate shutter is closed and the substrate holder is kept in the loading position.
- Select the Al crucible dedicated to grAl depositions and rotate the sample to the evaporation position. Insert an oxygen flow and slowly increase the current on the target to obtain the desired deposition rate. Once it is stable, open the shutter and evaporate the desired grAl thickness.
- Close the substrate shutter, stop the oxygen flow and ramp down the current on the Al target.
- Unload the metalized sample.

Although the granular Al evaporation process is relatively straightforward, there are limitations set by the components that need to be known before starting the recipe calibration. The first limitation is the maximum allowed pressure during evaporation. The value is set by the electron beam gun, which cannot stand pressures above 10^{-5} mbar during operation. In this sense, it is advisable to have a mass flow controller with 0.1 sccm precision or below. Mass flow controllers with higher ranges (e.g. 100 sccm) and precision on the 1 sccm can also be used when they are combined with deposition rates on the order of ~ 1 nm/s [Gei+24; Ihs+25]. An alternative to obtain a wider range of resistivities while keeping a relatively low evaporation rate with a 100 sccm mass flow controller is to introduce argon to reduce the partial pressure of oxygen in the chamber. Still, the system will be limited by the maximum allowed pressure during deposition. The second limitation is related to the maximum current allowed in the crucible pocket which will set a limit to the evaporation rate.

For our grAl calibration we use an evaporation rate of 0.2 nm/s and oxygen flows up to 0.8 sccm. A rate of 0.2 nm/s requires currents in the range 60 mA – 320 mA, depending on whether a liner is used in the crucible pocket or not. On the other hand, when a liner is not used, relatively low deposition rates (0.1-0.2 nm/s) appear to be more stable. The maximum flow is set by the pressure in the process chamber. For a standard grAl deposition in our Plasssys with 0.2 nm/s and 0.8 sccm, the pressure in the process chamber during deposition reaches around 2×10^{-6} mbar[1].

[1]The pressure during evaporation is actually lower than the pressure during the current ramp. During this process and with 0.8 sccm, we can reach up to 5×10^{-5} mbar which is close to the system's limit

Granular Aluminum characterization

Three DC test structures are used to characterize grAl (see right panel in Fig. 2.3). They are designed with a different number of squares and geometries to adapt to samples with a wide range of resistivity values. Additionally, the top two structures in Fig. 2.3 are convenient to perform temperature-dependent resistance measurements. They both have four relatively big pads which are suitable for wire-bonding in 4-probe configuration. In order to pattern different DC test structures, we use the optical lithography process described in Section 2.1.1. Devices are deposited on an intrinsic Si substrate previously cleaned with acetone and isopropanol.

We perform a set of grAl evaporations at different O_2 flows and measure the resulting structures with a 4-probe resistance measurement right after fabrication and after performing a thermal annealing of 13 min at 200 °C. In our qubit devices, grAl is the first EBL layer. During the Josephson junction and contact fabrication the sample undergoes a set of bakes with temperatures ranging from 150 °C to 190 °C and a total duration of approximately 13 min. The bake used in the calibration process is used to estimate the change of resistance due to the multi-layer fabrication process [Rot+16]. Figure 2.3 shows one of the grAl calibration curves for 50 nm-thick samples right after fabrication and after performing a 13 min at 200 °C bake. The sheet resistance increases non-monotonically with the addition of O_2 in the chamber. Annealing the sample reduces the resistance of the film by a $10-20\%$. Finally, note that those samples evaporated at 0.8 sccm are significantly less reproducible. This lack of reproducibility is due to difficulties to stabilize the rate at higher O_2 flows.

In this thesis, grAl will be used as a superinductor material to achieve large inductances in reduced volumes (see Ch. 3 and 4). Thus, to complete the calibration, it is important to obtain an estimate of the sheet kinetic inductance ($L_{\mathrm{k},\square}$) of the films as a function of other parameters. Using the Mattis-Bardeen formula for complex conductivity in the local, dirty limit at low frequency ($hf \ll k_B T$) and in the low temperature limit ($T \ll T_c$) we can obtain an estimate for $L_{\mathrm{k},\square}$ [Rot+16],

$$L_{\mathrm{k},\square} = 0.18 \frac{\hbar R_{4\mathrm{K},\square}}{k_{\mathrm{B}} T_{\mathrm{c}}}, \tag{2.1}$$

where T_{c} is the critical temperature, $R_{4\mathrm{K},\square}$ is the normal state sheet resistance measured at 4K and k_{B} is the Boltzmann constant.

The interesting $R_\square$ range in Fig. 2.3 comprises samples evaporated with 0.6 sccm. These samples display a small dispersion of resistance values and their resistance is an order of magnitude larger than Al ($R_{\square,\mathrm{Al}}^{\mathrm{Before}} = (0.89 \pm 0.06)\,\Omega/\square$). In Fig. 2.4, we present an example of a temperature-resistance curve for grAl prepared with 0.6 sccm (the details of these $R(T)$ measurements are presented in

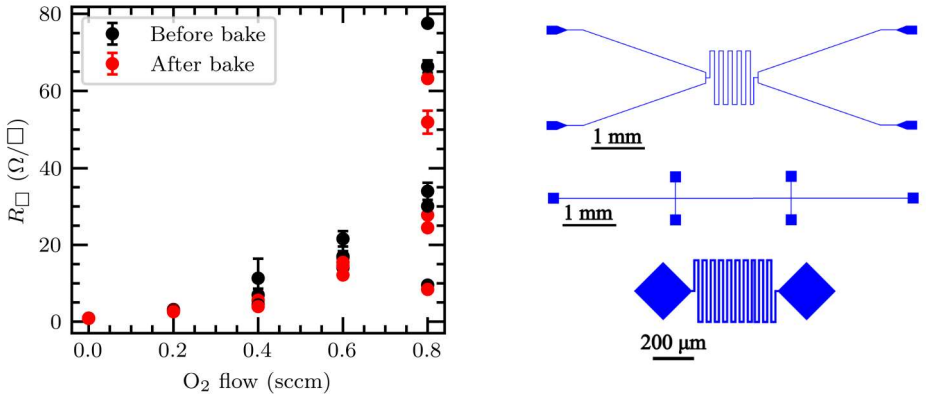

Figure 2.3: GrAl calibration for 50 nm thick samples evaporated at different O_2 flows. The black circles indicate the sheet resistance right after fabrication and the red ones show the sheet resistance after a bake of 13 min at 200 °C. The error bars indicate the spread of values between the different test structures present on each chip. The image on the right, shows different test structures used for the resistance measurements.

Ch. 5). The critical temperature for 0.6 sccm range is estimated around 2 K and the sheet resistance at 4 K is a factor 1.1 smaller than the room temperature sheet resistance $R_{\square,\mathrm{RT}}$. With this information and using Eq. (2.1), we can estimate the sheet kinetic inductance to be around $L_{k,\square} \sim 10\,\mathrm{pH}/\square$.

2.1.3 Qubit and junction fabrication

In this section, we will focus on qubit and Josephson junction fabrication based on electron beam lithography (EBL).

At the IFAE QCT group, we have developed a multi-step qubit fabrication recipe consisting on three steps for the devices presented in Ch. 4 and two steps for standard flux qubit designs. The qubit fabrication consists of grAl deposition, Josephson junction fabrication and contact layer deposition. Dividing the fabrication in multiple steps leads to flexible design geometries and clean contacts between Josephson junctions and other structures already present on the device. Particularly for the devices presented in Ch. 4, our multi-step fabrication allows for adjusting the design parameters after every step of fabrication to make sure the qubit-resonator system is in the USC regime. However, the versatility in our fabrication process comes at the expense of number of lithography, evaporation and cleaning steps. This is in contrast to the three-angle deposition method used

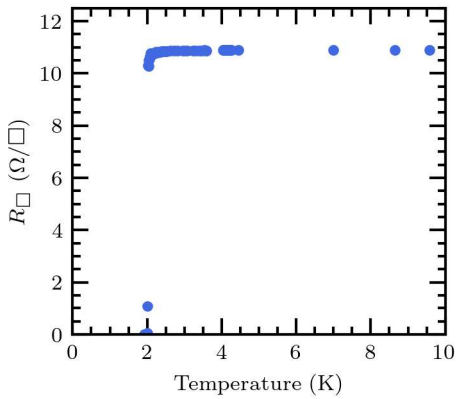

Figure 2.4: Example of T_c for a 50 nm grAl sample with $R_{\square,\mathrm{RT}} = 11.90\,\Omega/\square$ evaporated at 0.2 nm/s and 0.6 sccm of O_2 flow. The estimated critical temperature is $T_c = 2.01 \pm 0.01$ K.

in grAl-based fluxonium qubits where Josephson junctions and grAl are patterned in one EBL step and evaporated consecutively without breaking the evaporator vacuum [Grü+19; Grü19].

The workflow of our qubit fabrication can be summarized as follows:

1. EBL of grAl structures. Before deposition, we clean resist residues using an in-situ O_2 plasma descumming process. Afterwards, grAl is evaporated vertically and subsequently lifted-off.

2. Josephson junctions patterning with EBL. We clean resist residues using an in-situ O_2 plasma descumming step. Keeping the device in vacuum, the junctions are shadow-evaporated with an intermediate static oxidation step. The junctions are lifted-off right after evaporation.

3. Patterning of the contacts by EBL and cleaning of the resist residues using an O_2 microwave plasma ashing. We then perform an Argon ion milling step to ensure a clean and superconducting contact between the different layers of the chip. Finally, the contacts are evaporated in a vertical deposition.

It is essential to have a proper calibration and control of all the steps listed. In the following, we provide a detail of the fabrication process and characterization of Josephson junctions as well as the different intermediate cleaning steps.

Oxygen plasma and Argon ion milling

A proper substrate and metal layer cleaning is key to obtain reproducible devices. Resists such as PMGI SF7 are known to leave a substantial amount of residues, while chemicals like MP-351 (PMGI developer) are not sufficient to remove them. Plasma descumming is a technique used to remove organic residues. The effect of the descumming is to reduce the aging of Josephson junctions and to increase their reproducibility [Pop+12; Kop+07]. We have the capability of performing microwave oxygen plasma descumming in-situ prior to deposition inside the Plassys evaporator. Alternatively, we can use a dedicated TePlA GIGABatch 360M plasma asher machine at the CNM cleanroom. We characterized the descumming effect for both systems and for the different resists used for Josephson junction fabrication. We spin coat samples with CSAR62 and PMGI SF7 independently and dice them into several pieces. The thickness of the resist is measured after each plasma ashing recipe to find the optimal ashing rate.

For the TePlA system we use a recipe with 200 W of power and 50 sccm of O_2 flow. In Fig. 2.5 (a), we show the resulting ashed thickness as a function of time for both PMGI and CSAR. A simple linear fit to the data gives an estimated ashing rate of 40.2 nm/min for PMGI and of 25.4 nm/min CSAR. With ~ 30 s of recipe time should be sufficient to remove resist residues from the surface. The same process is repeated for the plasma descummming available at the Plassys evaporator. In this case, we use a recipe with 50 W of microwave power, 10 sccm of oxygen flow and a source frequency of 2400 MHz. The resulting etched resist thickness is shown in Fig. 2.5 (b). A linear fit to the data provides ashing rates for PMGI of 17.8 nm/min and 16.3 nm/min for CSAR. Similarly to the previous case, ~ 1 min should be enough to clean resist residues.

An additional key cleaning procedure we used in the junction fabrication procedure is the Argon ion milling. This process is usually employed to remove oxides from existing metal layers [Grü+17]. We use Argon ion milling before depositing the contact layer between the Josephson junctions and other metalized areas of the chip. The Plassys evaporator is equipped with a Kaufman ion source allowing us to run the 4 min ion argon milling process in-situ prior to metal deposition. The parameters of the ion source during cleaning are:

- 6 sccm Ar gas flow
- 400 V beam voltage
- 22 mA ion beam current
- 80 V ion beam acceleration voltage
- 40 V EBG discharge voltage

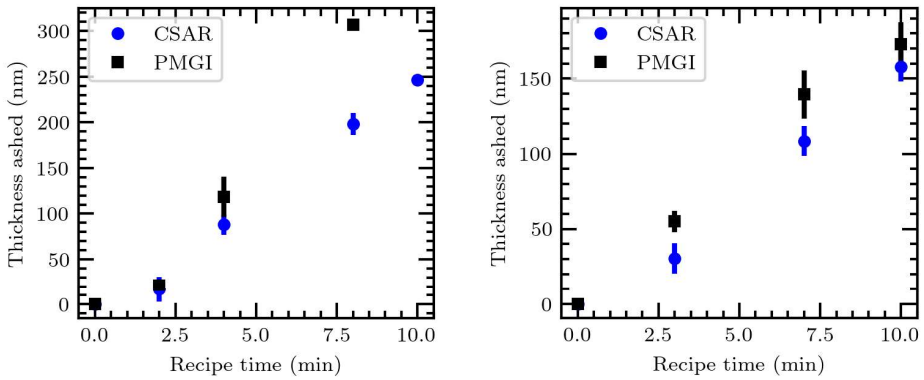

Figure 2.5: CSAR62 and PMGI SF7 resists thickness removed as a function of the descumming recipe time. (a) TePlA system with 200 W of power and 50 sccm of O_2 flow. (b) Plassys with 50 W of microwave power, 10 sccm of O_2 flow and frequency 2400 MHz.

Josephson Junction fabrication

At the IFAE QCT group we developed a recipe for the well-known Manhattan-style Josephson junctions [Pot+01]. We opted for a double-stack resist consisting of a bottom layer of PMGI SF7 of thickness 630 nm and a top layer of CSAR62 of thickness 240 nm. CSAR62 defines the dimensions of the junction leads and areas, while PMGI SF7 gives the necessary undercut for the shadow angle evaporation. The advantage of PMGI SF7 over other resists used for EBL lithography is that no ghost dose is needed to obtain a large enough undercut. The undercut in PMGI depends on the developer used, the development time and the pre-bake.

We pattern the Josephson junctions on a 30 kV Raith EBL system using 20 kV and a 20 µm aperture with a dose of 180 $\mu C\,cm^{-2}$. The samples are developed in two steps, first with a CSAR developer (AR 600-546) and, secondly, the PMGI developer (a solution of 1:3.5 $MP-351 : H_2O$). The detailed development process is given in Section A.4. As detailed in the previous section, prior to deposition, the sample undergoes an oxygen plasma descumming to remove organic residues on the substrate, mostly from PMGI.

The Josephson junction deposition is performed in an Al-dedicated Plassys evaporator following the steps:

- Pump the samples down overnight ensuring a load-lock pressure below 1.7×10^{-7}mbar, and a process chamber pressure below 5×10^{-8}mbar.

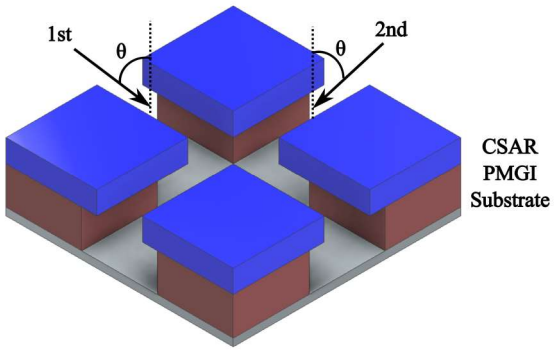

Figure 2.6: Schematics for the resist stack needed for Manhattan-style junctions. The blue layer simulates the CSAR62 resist and the dark brown represents the PMGI SF7. The different arrows indicate the two evaporation directions and θ represents the tilt angle.

- First evaporation at 55° tilt angle of 36 nm of Al at 0.3 nm/s rate.
- Static oxidation at 0.5 mbar.
- Second Al evaporation of 69 nm at 0.3 nm/s rate performed rotating 90° in the planetary direction and tilting the substrate 55°.
- Final oxidation step of 5 min at 0.5 mbar to passivate the electrodes and reduce ageing [Bil+21].

The Manhattan-style Josephson junction deposition is depicted in Fig. 2.6. The effective thickness in each evaporation step results in $\sim$ 20 nm and $\sim$ 40 nm, respectively. The effective thickness is calculated using $t_{\text{set}} \cos\theta$, where t_{set} is the thickness at the evaporator and θ the angle of evaporation. The latter expression can be obtained considering that the target thickness is measured in the vertical direction while the substrate during JJ deposition is tilted an angle θ (see for example Fig. 2.7).

Once the sample has been successfully evaporated, we perform the liftoff in a solution of N-methyl-2-pyrrolidone (NMP) at 75 °C with a stirring magnet set to a rotation of 150 rpm for 2 h. We finish the lift-off process by rinsing the sample in IPA and drying it with N_2. Our fume-hood is covered with an antistatic cage and equipped with an ion fan to avoid electrostatic discharges on samples.

Josephson junction areas and evaporation angle

The maximum and minimum Josephson junction areas are limited by the evaporation angle and the resist height and undercut.

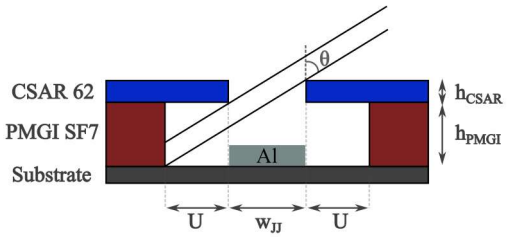

Figure 2.7: Schematics to determine the evaporation angle for Manhattan-style junction evaporation. θ is the angle of evaporation, w_{JJ} is the designed width of the Josephson junction, U is the undercut and h_{CSAR} and h_{PMGI} are the resist thicknesses of CSAR62 and PMGI SF7, respectively.

Using the schematics of Fig. 2.7, we can calculate the minimum angle needed to evaporate Manhattan-style junctions with our resist stack. Let us assume that the first Josephson junction layer has been deposited on the substrate (see the Al rectangle defined in the schematics). We want to obtain the minimum angle for which the Al from the second evaporation will be deposited on the resist wall. This condition will avoid a secondary lead of Al being deposited next to the one defining the Josephson junction. From a mathematical point of view this condition reads,

$$\tan\theta = \frac{w_{\mathrm{JJ}} + U}{h_{\mathrm{PMGI}} + h_{\mathrm{CSAR}}} \quad \Longrightarrow \quad \theta > \arctan\left(\frac{w_{\mathrm{JJ}} + U}{h_{\mathrm{PMGI}} + h_{\mathrm{CSAR}}}\right), \tag{2.2}$$

where h_{PMGI} and h_{CSAR} are, respectively, the thicknesses of the PMGI and CSAR resist layers, U is the undercut and w_{JJ} is the width of the first Josephson junction lead layer. Using a total resist thickness of $h_{\mathrm{PMGI}} + h_{\mathrm{CSAR}} = 870\,\mathrm{nm}$, the estimated undercut U which takes values between 500 nm and 700 nm and a maximum Josephson junction width of 300 nm, we obtain that the evaporation angle should be above $50°$ for $U = 700\,\mathrm{nm}$. The same idea can be used to calibrate the undercut of the resist, which can be determined by designing Josephson junctions of increasing width and evaporating them at a fixed angle. The maximum Josephson junction width will be given by the design that does not show a secondary lead. This width can be used in Eq. (2.2) to obtain an estimate of U.

The minimum Josephson junction width is mostly determined by the length of the Josephson junction lead, the possible angle loading error and the patterning

parameters. With the geometry described in this section and for 55° evaporation angles, we have been able to pattern 160 nm-wide Josephson junctions.

Josephson junction current density estimate

The fabrication process of Josephson junctions includes a static oxidation step at 0.5 mbar. The oxidation time determines the oxide barrier grown between Al leads and, thus, the properties of the Josephson junction [Mos+23]. In general, for flux qubit applications, we need Josephson current densities ranging between $2.0\,\mu\mathrm{A}/\mu\mathrm{m}^2$ and $3.0\,\mu\mathrm{A}/\mu\mathrm{m}^2$. We could also use dynamic oxidation for this range of current densities, but the dynamic oxidation pressures are limited to 0.05 mbar by the 10 sccm O_2 mass flow controller of our setup. Given the low pressures, the samples require between 30 to 40 min of dynamic oxidation to reach the desired target J_c. Instead, with static oxidation, we can reach similar values in a fraction of this time ($\sim 10\,\mathrm{min} - 15\,\mathrm{min}$). We use the structures depicted in Fig. 2.8 to calibrate the Josephson junction oxidation . The first three copies numbered 1-3 are used to calibrate the small Josephson junctions with areas given by αA with $0.5 < \alpha < 1$ (see Ch. 3 for more details on the selection of α). The remaining three copies are used to calibrate the big junctions of area A. The design also includes a vertical and a horizontal short to characterize the Al resistance in each of the two evaporation steps.

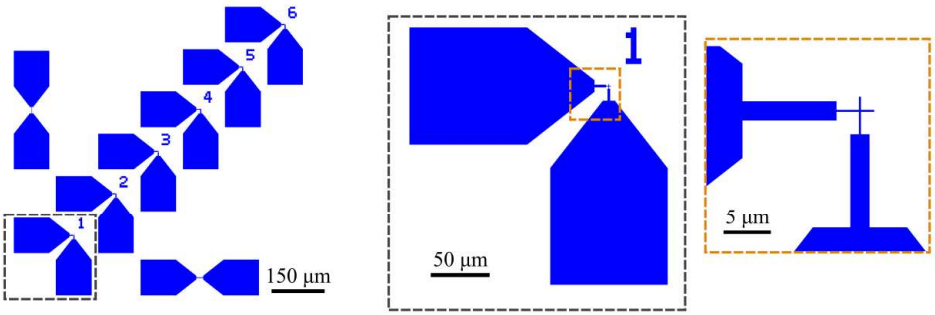

Figure 2.8: Design to test Josephson junction oxidation. Copies 1-3 are used to test the small junctions (αA), while copies 4-6 are used for the big junctions (A). The vertical and horizontal test structures visible in the left image are shorts to test the Al resistance in each evaporation.

Multiple Josephson junction oxidation pressure calibrations have been performed during the course of this thesis. In the following, we present the latest calibrations used for the fabrication of the device studied in Ch. 4.

One can estimate the Josephson junction critical current (I_c) through the Ambegaokar-Baratoff formula [Amb+63],

$$I_c R_n = \frac{\pi \Delta}{2|e|}, \tag{2.3}$$

where R_n is the junction normal state resistance, Δ is the gap of the superconductor and e is the electron charge. We can estimate the superconductor gap by using $\Delta \simeq \Delta_0 \simeq 1.764 k_B T_c$, where Δ_0 is the superconducting gap at zero temperature, and $T_c = 1.2\,\mathrm{K}$ is the critical temperature of Al. As a first approximation, and given the low RRR of our thin films, we use the room temperature resistance obtained by two-probe measurement (see Sec. 2.2 for a description of the setup) of the test junctions presented in Fig. 2.8. With this set of parameters, it is possible to estimate I_c. However, it is relevant to have access to the Josephson junction critical current density $J_c = I_c/A$, which requires an estimate of the junction area, A.

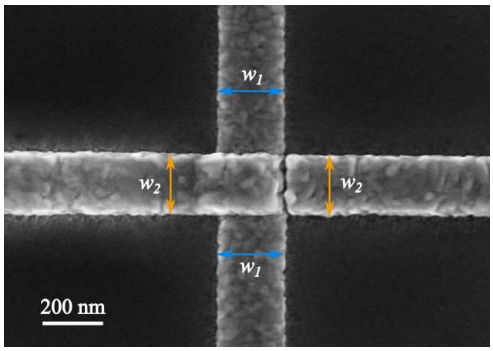

Figure 2.9: Example of a SEM image of a Josephson test junction. The blue and orange arrows indicate the regions used to determine the width of the different junction leads.

The resulting Josephson junction area can differ from the designed value and is strongly influenced by the quality of the EBL focus. In order to obtain a more accurate estimate of Jc, we acquire scanning electron microscope (SEM) images of the different test junctions. In Fig. 2.9, we show an example of a SEM image of a test junction. The blue and orange arrows indicate the regions used to determine the width of the different junction leads. Combining the measured widths (w_1, w_2) together with the nominal thickness of the bottom layer (t_1), we can determine the area of the Josephson junction,

$$A = w_1 w_2 + t_1 w_2. \tag{2.4}$$

Note that Eq. (2.4) considers the surface defined by the two crossing leads and the first edge contact connecting both layers. We neglect the contribution of the second edge contact since it is broken in a vast majority of devices (see the right junction contact in Fig 2.9). To achieve a complete contact from both sides of the Josephson junction a third evaporation angle of 55° tilt and −90° planetary rotation could be included in the deposition process.

Combining the resistance measurements at room temperature and the estimate of the Josephson junction area, we can finally calculate J_c. In Fig. 2.10, we show the resulting set of values obtained for test junctions fabricated with a static oxidation at 0.5 mbar and different oxidation times. Each point represents the averaged J_c for a test junction chip containing four copies of the structures presented in Fig. 2.8. Panel (a) shows J_c obtained for big Josephson junctions ($A \sim 0.078\,\mu m^2$) while panel (b) shows J_c values for small junctions ($A \sim 0.045\,\mu m^2$). We show less points for small Josephson junctions, given that they were breaking more easily due to a slight change in EBL dose factor calibration. We plot together Josephson junctions fabricated with (purple and gray) and

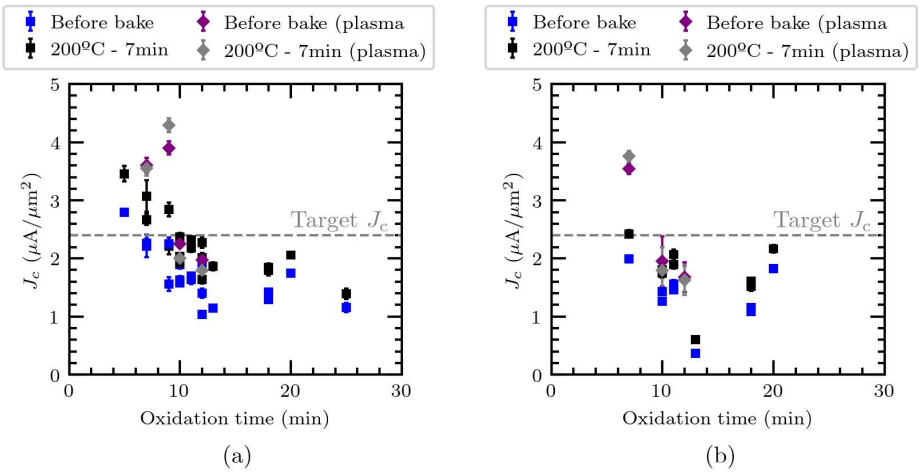

Figure 2.10: Estimated Josephson junction critical current density as a function of the oxidation time for a static oxidation pressure of 0.5 mbar. In blue/purple we show the data obtained right after fabrication, and in black/gray the J_c after a bake of 200 °C for 7 min. Samples corresponding to purple and gray markers underwent an O_2 plasma descum before deposition. The dashed gray line indicates the target $J_c = 2.4\,\mu A/\mu m^2$ value for the design studied in Ch. 4. (a) Estimated J_c for big Josephson junctions ($A \sim 0.078\,\mu m^2$) and (b) estimated J_c for small Josephson junctions ($A \sim 0.045\,\mu m^2$).

without (black and blue) an O_2 plasma descumming step. In general, Josephson junctions fabricated without an O_2 descumming show a higher change in resistance and J_c with a 200 °C bake of 7 min. This significant change in resistance can be linked to resist residues in the vicinity of the junction [Pop+12; Kop+07]. Besides the change in resistance observed after the bake, we also observe a significant spread of J_c values. We attribute the spread of J_c to problems in the rate stabilization during evaporation and changes in the process chamber pressure. Additionally, environmental conditions such as temperature and humidity are not always well controlled and may have an effect on Junction reproducibility.

The calibration of the Josephson junction current density could be improved further. From a fabrication point of view, it is clear that cleaning the substrate before deposition has an impact on the resistance and aging of junctions, thus O_2 descumming needs to be included in the fabrication process. On the other hand, creating a new curve each time the process chamber of the evaporator is opened or setting lower and consistent pressure thresholds before evaporation can help reduce the spread in each calibration curve. By better controlling other ambient elements such as temperature or humidity fluctuations in the cleanroom we can also reduce the spread in junction resistance. Similarly, the spread in area could be improved by introducing a cold development. This process ensures a reproducible temperature of the developer and it is known to yield consistent and reproducible areas [Mil22]. Finally, a possible way in which the Al grain size can be standardized by better stabilizing the evaporation rates. This can be achieved by a proper melting of the crucible metal and a proper allocation of the beam spot.

Fabrication of contacts

The last fabrication step in our qubit recipe consists of patterning and evaporating patches connecting the different metal layers. Previous works [Osm+21] have proposed a method to evaporate the contacts in-situ after junction deposition. However, this process requires thick resist stacks and the calibration of a three-angle shadow evaporation. We decided to follow the standard approach which consists of adding an extra EBL step. On the other hand, this is by far the most common procedure in the community [Dun+17].

In the patch fabrication step we change the resist stack. Instead of PMGI SF7 and CSAR 62, we use MMA EL6 for the bottom layer and PMMA 950 A4 for the top layer. The change of resist stack is motivated for two reasons. First, the increased resistance measured in test junction structures with patches fabricated in PMGI and CSAR. The bad contact is probably due to resist residues in the different metal surfaces left by PMGI. Secondly, the particular stack of MMA EL6 - PMMA 950 A4 used in this work can be patterned at 10 kV. Decreasing the voltage and dose near the Josephson junctions can decrease significantly the

impact on the final resistance due to stray back-scattered electrons [Bal+24].

The evaporation of the contacts requires two separate cleaning procedures. First, an oxygen plasma descumming to remove possible resist residues and, secondly, an Argon ion milling step prior to deposition to eliminate surface oxides. In order to avoid the contacts from breaking, we deposit a total Al thickness of at least 100 nm. This thickness is twice the value used for the optical layer and two to four times thicker than the different junction leads. We validate the quality of the contacts on the same device by measuring Josephson junctions fabricated with patches and comparing them with single-step junctions.

2.2 Experimental setup

In this section, we present the setup used for the experiments detailed in Ch. 4 and 5. We also provide some details on the room-temperature characterization setup used for the calibrations presented in Sec. 2.1.2 and 2.1.3.

2.2.1 Room temperature characterization setup

For room-temperature measurements we employ two-probe or four-probe techniques. In both, we use a manual probe station. For the 4-probe measurements of metal structures or thin films, we use a Keithley 2634B source meter. For Josephson junction characterization, we use 2-probe measurements. In this case, we use a digital Keithely multimeter connected to a home-built *Josephson junction measurement box*. The purpose of this box is to regulate the maximum current bias applied to the Josephson junction by fixing the voltage across the junction to 10 mV.

2.2.2 Qubit and DC measurement setup

The experimental setup used for the qubit measurements and thin film resistance measurements respectively presented in Ch. 4 and 5 is summarized in Fig. 2.11. The setup consists of a BlueFors SD cryogen-free dilution refrigerator equipped with three radio frequency (RF) lines and 24 DC lines. Input 1 is used to drive the sample with a microwave tone, input 2 has less attenuation and it is used to send flux pulses to the qubit control line and, finally, the output line is used to read the transmitted signal through the sample. Besides the difference in attenuation, the last stages of the output line are made of Ag-CuNi cables with Ag center line which decrease the signal loss at the cost of less thermal isolation. The DC lines are used to either drive a coil attached to the sample box, or to perform thin film resistance measurements. In the former case, the DC lines are made from phosphor-bronze until the 4 K stage. From 4 K down to the

mixing chamber, they are uninterrupted and made from CuNi-NbTi not to break superconductivity. For thin film resistance measurements, the DC lines are made entirely out of phosphor-bronze.

Background magnetic fields are screened by a combination of three shields:

- Flexible mu-metal lamina that covers all the surface outside the vacuum.
- A 2 mm-thick mu-metal shield inside the vacuum can expected to provide a 250 factor of attenuation over the Earth's magnetic field.
- A 2 mm-thick Pb shield is installed inside the still can.

The Pb shield provides screening against gamma ray radiation and takes advantage of the fact that Pb is a superconductor below 7.2 K, thus, magnetic fields are expelled by the Meissner effect. The combination of shields is expected to provide a total factor 2×10^5 of attenuation over the Earth's magnetic field.

For qubit experiments the sample is mounted and wire-bonded to a 6-port ceramic PCB and packaged inside a light-tight copper sample box. Below the PCB, a thin rectangular copper piece is used to improve the thermal contact between the sample box and the PCB. Finally, in qubit measurements we usually include a copper spacer to reduce the number of parasitic box-modes (see Fig. 2.13). The sample box is then mounted on the mixing chamber (MXC) stage, reaching ~ 20 mK. In Fig. 2.12 we show a picture of a qubit sample mounted in the dilution refrigerator. For temperature dependent resistance measurements of thin film superconductors, we use commercial non-magnetic chip carriers from Kyocera that can be mounted either on the still or the mixing chamber plate.

Qubit measurements

The qubit presented in Ch. 4 is characterized mainly by spectroscopy measurements use two types of instruments. First, an Agilent E5071B VNA Network Analyzer (300kHz - 8.5GHz) sends a continuous RF tone and reads the transmitted and/or reflected scattering signals. Generally, the signal is attenuated between the VNA output and the sample box by $\simeq 120$ dB to reach the single-photon level at the sample (~ -140 dBm). The second instrument used in spectroscopy measurements is the RF-source able to send tones at GHz frequencies. In our case, we use a Rohde & Schwarz SGS100A SGMA.

We use two types of qubit spectroscopy techniques widely spread in the superconducting qubit community: single-tone spectroscopy, and two-tone spectroscopy. These measurements consider a system of a qubit coupled to a readout resonator, similarly to the experiment presented in Ch. 4. In single-tone spectroscopy one measures the transmission of the RF VNA tone as the magnetic flux at the qubit is swept using a superconducting coil. By changing the current

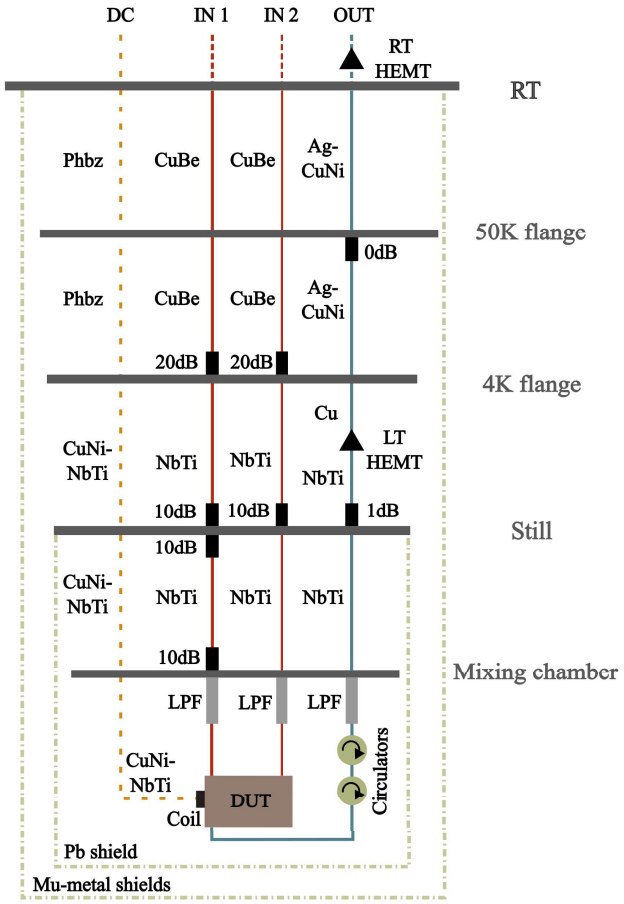

Figure 2.11: Schematics of the dilution refrigerator cabling for qubit and thin film resistance measurements. The material of each cable is indicated next to the line. Phbz stands for phosphor-bronze LT and RT HEMT are the low-temperature and room-temperature microwave HEMT amplifiers, respectively LPF stands for low-pass filters and DUT is the device under test.

in the coil, we tune the magnetic flux through the qubit loop while scanning in frequency with the VNA. The second type of spectroscopy is the two-tone measurement. In this case, we fix the VNA frequency tone at the resonator's resonant frequency while a second tone generated by the RF-source is scanned to

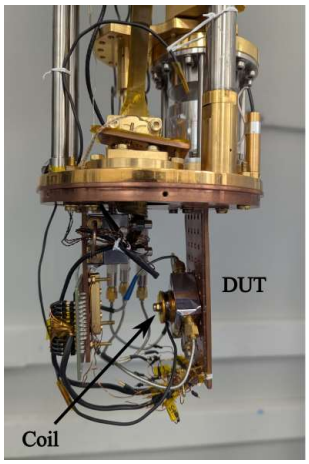

Figure 2.12: Image of the mixing chamber stage wiring. The sample box is mounted on the rightmost bracket. The different RF lines are connected to the side connectors of the sample box and the superconducting coil is screwed on the top lid.

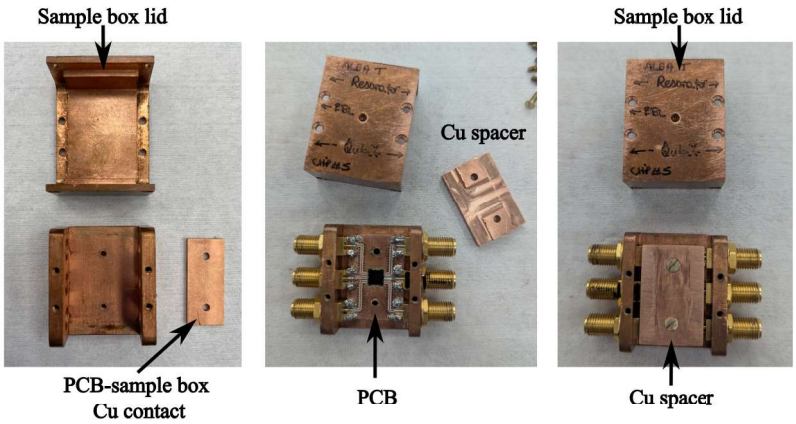

Figure 2.13: Images describing the assembly of the sample box. The Cu spacer piece is used to fill empty space and to avoid unwanted box modes.

search the qubit frequency. When the RF-source frequency matches the qubit, a shift in the resonator transmission amplitude is observed, as the excitation of the

qubit produces a state-dependent dispersive shift in the resonator which depends on detuning and coupling. One can obtain the qubit spectrum by running this measurement as a function of the magnetic flux. A detailed description of qubit measurements and the setup used in the group can be found in the PhD work of [Lóp24].

Chapter 4

Superinductive ultrastrong couplings: Experiments

Alba Torras-Coloma, Luca Cozzolino, Ariadna Gómez-del-Pulgar-Martínez, Elia Bertoldo and P. Forn-Díaz

Contents

4.1 Design of a qubit-resonator system in the ultrastrong coupling regime 96
4.1.1 Resonator design 98
4.1.2 Qubit design 100
4.1.3 Coupled system 104
4.2 Spectrum characterization 106
4.2.1 Room temperature and grAl characterization 106
4.2.2 Low-temperature transmission measurements 108
4.2.3 USC spectrum discussion 116
4.3 Outlook 119

In this chapter, we present the design and measurements of a 3-junction flux qubit galvanically coupled to an LC oscillator, as introduced in Ch. 3. The circuit design has two distinctive features. First, we use a superinductor material as a shared coupling element between the flux qubit and the resonator and, secondly, we include two feedlines into the design to independently probe the system through either the qubit or the resonator.

The experimental data shown in this chapter corresponds to a sample with significantly off-target parameters, but still, in an interesting regime. In particular, the fits to the Quantum Rabi model reveal that despite the low persistent current of the qubit, the qubit-resonator coupling is in the perturbative USC regime. The results validate the use of superinductors as an approach to reach

ultrastrong galvanic couplings while keeping qubit parameters in a range compatible with long coherences [Tor+25]. In addition, the experiment serves as a proof of concept for studies in the USC regime with multiple probing lines. The incorporation of superinductors in qubit circuits opens the door to new USC designs and studies using low persistent current qubits, hence higher coherence, and large superinductive galvanic couplings.

4.1 Design of a qubit-resonator system in the ultrastrong coupling regime

In Ch. 3, we have presented the electrical circuit and the Hamiltonian to study a flux qubit galvanically coupled to an LC oscillator in the USC regime. In this section, we present the design parameters and design layout used to implement the experiment.

Before diving into the design, we can give some insights on how to reach the USC regime with flux qubits and resonators. Recall the approximate expression for the coupling coefficient derived in Section 3.3.3 in the limit $\tilde{\alpha}C_J \ll C_R$,

$$g \simeq \xi_{R,A}\frac{L_\mathrm{c}L_R}{L_\mathrm{c}+L_R}\frac{I_\mathrm{p}I_\mathrm{rms}}{\hbar} = \xi_{R,A}\frac{L_\mathrm{c}L_R}{L_\mathrm{c}+L_R}\frac{I_\mathrm{p}}{\hbar Z_R}\sqrt{\frac{\hbar\omega_R}{2C_R}}, \tag{4.1}$$

where $\xi_{R,A} = \sqrt{\omega_R/\omega_A}$ with ω_A the lowest normal mode frequency of the coupled harmonic system and $\omega_R = 1/\sqrt{L_\mathrm{R}C_\mathrm{R}}$ the frequency of the bare LC resonator[1].

In order to increase the coupling we should target low-impedance resonators, large persistent current qubits and large coupling inductors. The first two require adjusting the parameters of the resonator and the qubit. However, designing large and linear inductors is not simple. Most of the literature concerning flux qubits galvanically coupled to resonators or waveguides in the USC regime used Josephson junctions as couplers [Nie+10; For+17; Yos+17b; Yos+17a]. Junctions have the advantage that they can provide a large inductance in a small space and they are relatively easy to fabricate and include in qubit designs. Although Josephson junctions are simple to fabricate, errors in the area and critical current can lead to inaccurate inductance values of up to a $\pm 10\%$. Junctions also present a number of technical complications. They introduce stray nonlinearities which impacts the device functionality, while adding junction losses coming from quasiparticle tunneling [Ris+13] and two-level system defects [Bil+17]. Other studies

[1] Throughout this chapter we will use $\omega_R = 1/\sqrt{L_\mathrm{R}C_\mathrm{R}}$ to refer to the bare LC resonator, ω_A for the renormalized resonator frequency obtained with Eq. (3.39) which includes the effect of L_c and the capacitance of the α junction, and finally, ω_r to describe the resonator mode in the QRM without approximations.

proposed the use of shared thin Al wires to reach ultrastrong couplings [For+10]. However, reaching coupling strengths beyond the perturbative USC regime requires significantly long and narrow Al wires which can be challenging from a fabrication point of view. Alternatively, one would require loop lengths of tens or hundreds of microns, leading to an enhancement of flux noise.

The alternative explored in this thesis are superinductor materials. Superinductor materials are disordered superconductors that can reach characteristic impedances of the order of the resistance quantum $R_Q \sim 6.5\,\mathrm{k}\Omega$ [Man12] which essentially translates in large surface kinetic inductance. The advantage of these materials compared to junctions is their small nonlinearity combined with low microwave losses.

For our design we choose granular Aluminum (grAl) as the desired superinductor material. GrAl allows us to design inductances of the order of nH in relatively small spaces [Grü+18; Zha+19]. Furthermore, it is relatively easy to implement in Al-based fabrication processes [Grü+19]. The second distinctive element of this work consists of two individual feedlines on chip: one coupling to the qubit and the other one to the resonator. Fig. 4.1 presents the final circuit design as a guide for the reader. The top feedline couples to the capacitive part of the lumped element resonator. A flux bias line (FBL) controls the flux qubit. At the the bottom of the image, the qubit feedline couples to the qubit shunt capacitor. In the upcoming subsections we provide the design details for each element on the chip.

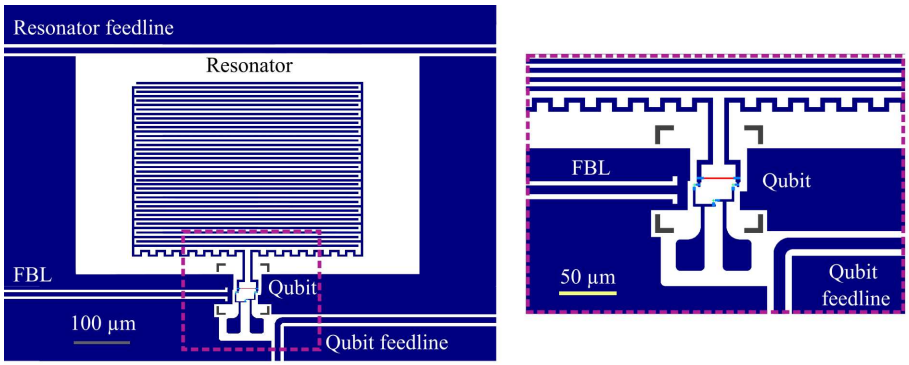

Figure 4.1: Device layout consisting on a three-junction flux qubit galvanically coupled to an LC lumped-element resonator with two feedlines and a flux-bias line (FBL). The panel on the right provides a zoomed in image of the qubit region.

4.1.1 Resonator design

We employ a lumped-element LC resonator for this experiment, which is a circuit smaller in length than the electromagnetic wavelength, where the current and voltage do not significantly vary over the dimensions of the inductor and capacitor, respectively. Therefore, lumped-element resonators display a single resonance mode [Poz21]. This is particularly relevant in our experiment where we want to couple only one electromagnetic mode to the qubit.

To simulate the resonator we use the 3D-planar high-frequency electromagnetic simulation software *Sonnet*[2]. A typical simulation layout of the LC resonator is shown in Fig. 4.2 with the circuit simulation parameters given in Table 4.1. Since our devices will be fabricated with 50 nm of Al we need to consider the kinetic contribution to the inductance by adding a sheet inductance of $L_\mathrm{s} = 0.4\,\mathrm{pH}/\square$ [Lóp+25] into the simulations. The capacitance (C_R) and total inductance ($L_\mathrm{R} = L_\mathrm{geo} + L_\mathrm{kin}$) of the resonator are estimated using the method described in [Doy+08; Lóp24], where a square of metal with sheet inductance L'_s is added into the resonator layout. This sheet inductance modifies the resonance by $\omega'_R = \frac{1}{\sqrt{(L'_\mathrm{s}+L_\mathrm{R})C_\mathrm{R}}}$. The values for L_R and C_R are extracted comparing ω'_R with $\omega_\mathrm{R} = \frac{1}{\sqrt{L_R C_R}}$.

Table 4.1: Sonnet resonator simulation parameters. We consider a general metal model with sheet inductance L_s estimated for 50 nm Al using the data in [Lóp+25]. The substrate is intrinsic silicon with t the thickness, $\tan\delta$ the dielectric loss tangent, σ the conductivity, ϵ_r the relative electric permitivity and μ_r the relative magnetic permeability.

Metal model	L_s (pH/□)	Si t (μm)	ϵ_r	$\tan\delta$	μ_r	σ (S/m)
General (lossless)	0.4	500	11.45	5e-5	1	0

In general, we want the resonances of our complete system to fall in the range 4 GHz and 8 GHz, which is imposed by the microwave components of our setup (see Sec. 2.2). For example, the low-temperature amplifier works best in the $4-8$GHz bandwidth and the low-pass filters have a cutoff frequency of 8 GHz. We target a resonator resonance frequency around 6 GHz which is considerably above 4 GHz. As shown in Sec. 3.3, we have to take into account that the coupling will renormalize the resonance frequency of the resonator to ω_A given by Eq. (3.39). The resulting capacitor geometry consists of 38 fingers of width 4 µm spaced 4 µm. This provides an estimated capacitance of $C_\mathrm{R} \simeq 0.74\,\mathrm{pF}$. The inductor is designed with a total of 28 legs of width 4 µm and length 4 µm. Two central legs are designed longer to accommodate the qubit.

[2]https://www.sonnetsoftware.com/

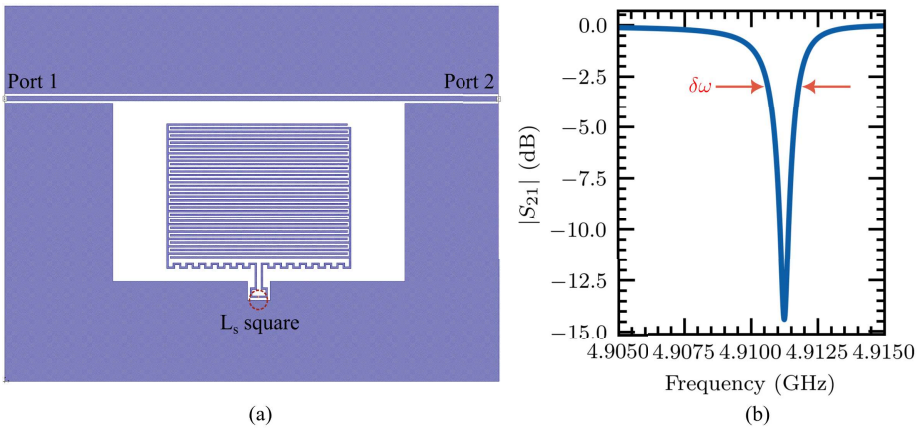

Figure 4.2: (a) Snapshot of a *Sonnet* simulation layout. The ends of the feedline contain the two different ports of the simulation, and the center of the long leg inductor contains an extra sheet inductance L_s to emulate the coupling inductor to the qubit. (b) Example of a resonance obtained setting $L_s = L_c = 0.5\,\text{nH}$ with $Q_L = 5 \times 10^3$ and $\delta\omega = 1\,\text{MHz}$.

The estimated resonator inductance from simulations is $L_R = 0.90\,\text{nH}$. Note that this value contains the sheet kinetic inductance of the Al [Lóp+25]. Considering the simulated inductance and capacitance, the resonator frequency is estimated to be $\omega_R/2\pi = (2\pi\sqrt{L_R C_R})^{-1} = 6.2\,\text{GHz}$. Note that ω_R is obtained without considering the effect of L_c and the total capacitance of the small qubit junction.

Recall that in the complete circuit design, the resonator will couple to the qubit through a shared inductance L_c. As we show in Sec. 4.1.2, a coupling inductor $L_c = 0.5\,\text{nH}$ is enough to bring the qubit-resonator system in the non-perturbative USC regime. If we take into account $L_c = 0.5\,\text{nH}$ into the resonator, the resonance is modified to $\omega_A/2\pi = 4.9\,\text{GHz}$. The renormalized resonator frequency ω_A is still above 4 GHz as we initially intended.

Coupling to the feedline

Another important parameter to consider is the resonator loaded quality factor, defined as

$$\frac{1}{Q_L} = \frac{1}{Q_{ext}} + \frac{1}{Q_{int}}, \tag{4.2}$$

where Q_{int} is the internal quality factor and Q_{ext} is the external quality factor. Q_L gives an idea of the losses of the system, and whether they are limited by the

coupling to the external circuitry (Q_{ext}) or by internal loss mechanisms (Q_{int}).

The internal quality factor can be estimated from the dielectric loss tangent of silicon at low temperatures, by $1/Q_{\text{int}} \approx \tan\delta$. Using literature values [Kru+06; Che+22] it is safe to assume a value of $Q_{\text{int}} = \frac{1}{\tan\delta} = \frac{1}{5\times10^{-5}} > 2\times10^4$, as used in Table 4.1 for our resonators. On the other hand, the external quality factor will be given by the coupling to the feedline. We estimate Q_{L} using the resulting S_{21} curve from *Sonnet* simulations and the width $\delta\omega$ at $-3\,\text{dB}$ of the resonance. Considering $L_{\text{c}} = 0.5\,\text{nH}$ in the resonator simulation and a distance of $52\,\mu\text{m}$ to the feedline, we obtain $Q_{\text{L}} \approx 5000$ while keeping a narrow enough bandwidth of $\delta\omega_{\text{r}} \simeq 1\,\text{MHz}$, and $Q_{\text{ext}} \approx 6500 \ll Q_{\text{int}}$. We expect the resonator to be overcoupled, as is usual in circuit QED readout resonators, while keeping an expected lifetime of $\tau = Q_L/\omega_A = 0.2\,\mu\text{s}$ compatible with a long enough coherence for this experiment.

4.1.2 Qubit design

We consider a 3-junction flux qubit where one of the junctions is an α factor smaller than the other two. Since the qubit will be coupled to the resonator by a shared inductor, we add L_{c} into the qubit simulations. A set of requirements that need to be fulfilled by the qubit in order to carry out this experiment:

- The flux qubit has to be in the double-well potential regime.
- The qubit gap ($\Delta_{\text{q}}/2\pi\hbar$) has to be close to $4\,\text{GHz}$
- The qubit should have a considerably large persistent current ($I_{\text{p}} > 50\,\text{nA}$). However, flux qubits with large persistent currents are more sensitive to flux noise [Yan+16]. Thus, we want to keep I_{p} on the lower side to maintain a compromise between qubit coherence and qubit-resonator coupling.

Besides these requirements, fabrication imposes a set of limitations. The area of the junctions will be mostly limited by the double-stack resist and evaporation angles presented in Ch. 2. We can fabricate junction areas (A) approximately between $0.03\,\mu\text{m}^2$ and $0.09\,\mu\text{m}^2$. On the other hand, the critical current density (J_{c}) will be limited by the area and the calibration of the junction oxidation. For our designs, we will target values of J_{c} between $2.0\,\mu\text{A}/\mu\text{m}^2$ and $3.0\,\mu\text{A}/\mu\text{m}^2$.

We can use Eq. (4.1) to give us an idea of the qubit parameters needed to reach the USC regime. Using the resonator designed in Sec. 4.1.1, by fixing the coupling inductance to $L_{\text{c}} = 0.5\,\text{nH}$ and the qubit persistent current to $I_{\text{p}} \approx 55 - 65\,\text{nA}$, we reach the non-perturbative USC regime. Performing a parameter sweep in the simulations, we obtain the qubit parameters listed in Table 4.2 fulfilling the set of requirements. The estimated persistent current for this qubit design is $I_{\text{p}} = 72.4\,\text{nA}$, with the calculated energies $E_J/h = 93.5\,\text{GHz}$ and $E_C/h = 4.9\,\text{GHz}$

for the large qubit junctions. The ratio of energies designed $E_J/E_C \gg 1$, ensures a low charge sensitivity. The resulting energies and spectrum for the qubit are shown in Fig. 4.3.

Table 4.2: Qubit design parameters. J_c and S_c are the current density and capacitance density of the junction, A is the area of the big junction, α gives the ratio in areas between the small and big junctions, C_{sh} is the shunt capacitor of the small junction, L_c is the coupling inductance and Δ_q is the qubit gap. S_c is estimated, the other parameters are simulated or directly measured.

J_c (μA/μm^2)	S_C (fF/μm^2)	A (μm^2)	α	C_{sh} (fF)	L_c (nH)	Δ_q/h (GHz)
2.4	50	0.0784	0.58	7.3	0.5	3.6

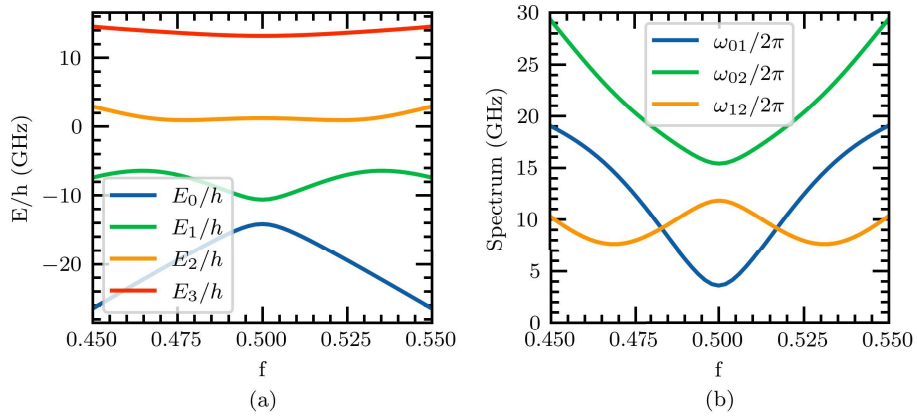

Figure 4.3: (a) Energies and (b) spectrum for the designed 3JJ qubit with L_c as a function of the external flux $f = \Phi_{ext}/\Phi_0$. The design parameters are listed in Table 4.2. The energies and spectrum are obtained by adapting the standard diagonalization method (see Sec. 3.4.1) to the Hamiltonian in Eq. (3.1).

Capacitance design

In this experiment the circuit contains two transmission lines to probe the qubit or the resonator independently. Since the space around the qubit is limited, we couple the qubit capacitively to the feedline using the shunt capacitor C_{sh} pads (see the bottom line in Fig. 4.1). In order not to limit excessively the coherence of our qubit, and at the same time obtain enough signal, we target a coupling capacitance to the line of $C_c = 0.4\,\text{fF}$. Using the approach derived in Sec. 3.5.1,

we estimate $T_1 \approx 10\,\mu s$ which is significantly low for the standards of flux qubits [Yan+16]. It would be possible increase T_1 by considering larger C_{sh} capacitors or reducing further C_c. However, an increase in C_{sh} normally implies reducing the qubit gap which would bring the qubit away from the resonator frequency. Overall, obtaining the ideal set of qubit parameters leads to a tradeoff between resonance condition, signal amplitude and qubit coherence.

The C_{sh} and the capacitance to the line C_c are estimated using the finite element simulation software *COMSOL Multiphysics*[3]. To extract the final capacitance of the different circuit elements, we perform a similar capacitance network analysis to the one described in [Lóp24]. We iterate this process by changing the dimensions and shapes of the capacitors until the obtained capacitance from *COMSOL* and the network analysis matches the value set on the qubit numerical simulations. For this particular case, the qubit capacitor pads are desigend to be $25\,\mu m \times 27\,\mu m$ spaced $16\,\mu m$. The distance from the edge of the capacitor to the central conductor of the feedline is set to $d_{Qf} = 19.5\,\mu m$ (see the schematics in Fig. 4.4).

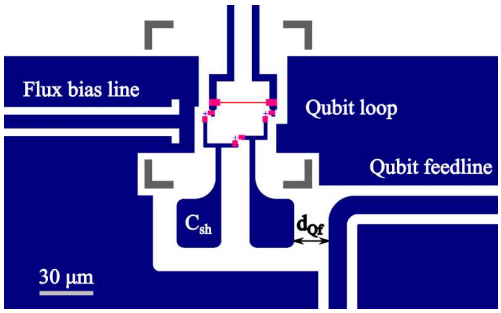

Figure 4.4: Flux qubit-resonator design zoomed around the qubit loop. The distance between the C_{sh} pad and the qubit feedline is given by the black arrow with $d_{Qf} = 19.5\,\mu m$.

Coupling inductor length

As previously discussed, the coupling inductor is fixed at $L_c = 0.5\,nH$. The choice of this inductance value is motivated by two reasons. First, our grAl recipe is calibrated and works best for samples evaporated with 0.6 sccm and 0.2 nm/s, leading to $L_{k,\square} \sim 10\,pH/\square$. Secondly, we cannot make arbitrarily large qubit loops or arbitrarily narrow and long wires. Big qubit loops will introduce flux

[3] https://www.comsol.com/

noise into our system, while designing long and narrow wires will translate into a lower fabrication yield.

If we take $L_c = 0.5\,\text{nH}$ and $L_{k,\square} \sim 10\,\text{pH}/\square$ we need about 50 squares of grAl. If we consider a qubit loop length of $\sim 30\,\mu\text{m}$ the design width of the grAl line will be of approximately $0.6\,\mu\text{m}$. This value gives room to adjust the grAl line to wider/narrower values if we see a drastic change in the calibration of the material.

Flux bias line design

We design the flux bias line (FBL) in *FastHenry*[4] which is a finite-element solver for the London equations at low frequencies. The qubit loop dimensions are given by the coupling inductor ($30\,\mu\text{m}$) and the Manhattan-style junctions ($18-22\,\mu\text{m}$).

The position of the FBL is determined by sweeping the location of the qubit in *FastHenry* as shown in Fig. 4.5. We target a mutual inductance between the line and the qubit of about $M = 0.1 - 0.2\,\text{pH}$ which occurs for $d_y = -0.5\,\mu\text{m}$ and $d_x = 18\,\mu\text{m}$. Note that the vertical and horizontal shifts are taken with respect to the center defined by the two top junctions and the lowest lead of the central junction. The choice of center is arbitrary and depends on the coordinates and geometry defined in the simulation.

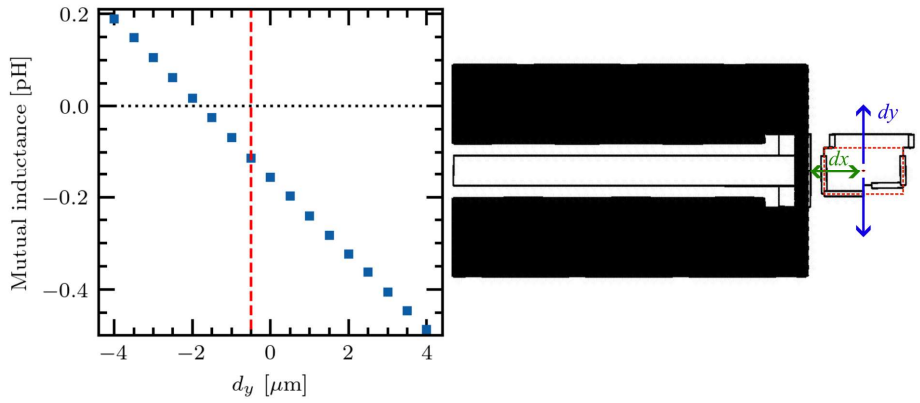

Figure 4.5: Left panel: simulated mutual inductance between the flux bias line and the qubit loop for $d_x = 18\,\mu\text{m}$, the red vertical dashed line indicates the selected design distance $d_y = -0.5\,\mu\text{m}$. Right panel: FastHenry simulation layout. The dashed red lines indicate the rectangle that defines the reference central point of the qubit loop.

[4] https://www.fastfieldsolvers.com/

The flux bias line adds a new loss mechanism into the qubit system since it is coupled to a resistive element such as the attenuator at the MXC plate. Following the lines of [Ith+05], one can estimate the qubit energy relaxation rate $\Gamma_{1,\mathrm{ind}}$ and dephasing rate $\Gamma_{\Phi,\mathrm{ind}}$,

$$\Gamma_{1,\mathrm{ind}} \approx \pi \left(\frac{2I_\mathrm{p}}{\hbar}\frac{\Delta_\mathrm{q}}{\omega_q}\right)^2 \left|\frac{M}{R+i\omega L}\right|^2 2R\hbar\omega \coth\left(\frac{\hbar\omega}{2k_\mathrm{B}T}\right), \tag{4.3}$$

$$\Gamma_{\phi,\mathrm{ind}} \approx 4\pi k_\mathrm{B}T \left(\frac{2I_\mathrm{p}}{\hbar}\frac{\epsilon}{\omega_q}\right)^2 \frac{M^2}{R}, \tag{4.4}$$

where I_p, Δ_q are the persistent current and the gap of the qubit respectively. ω_q refers to the frequency of the qubit at the operational point, M defines the mutual inductance between the flux line and the qubit, R and L are the real impedance and the inductance of the line, respectively, and T is the attenuator's temperature.

Considering $R = 50\,\Omega$, $L = 3\,\mathrm{nH}$, $M = 0.2\,\mathrm{pH}$, $\Delta_\mathrm{q}/h = 3.6\,\mathrm{GHz}$, and $I_\mathrm{p} = 72.4\,\mathrm{nA}$, operated at the sweetspot at $T \simeq 100\,\mathrm{mK}$, we obtain a minimum $T_1 \simeq 1.5\,\mathrm{ms}$, which is well above the limiting value imposed by the coupling to the qubit readout feedline. To estimate $T_{\phi,\mathrm{ind}}$ we choose a point far from the qubit sweetspot such that $\omega_q = \epsilon$. We obtain a value $T_{\phi,\mathrm{ind}} \simeq 40\,\mu\mathrm{s}$. This value looks rather low, but note that it is a point far from the sweetspot, where $I_\mathrm{p} \to \infty$

4.1.3 Coupled system

So far, we have been using the approximation in Eq. (4.1) as a guide to estimate the coupling coefficient from the individual parameters of the system. In order to give a proper estimate of the coupling coefficient we need to perform the complete numerical simulation of the system and calculate g from Eq. (3.31). In Fig. 4.6b, we provide the coupling coefficients as a function of the external flux. At the sweet-spot ($f = 0.5$) the coupling component is entirely transversal with value $g/2\pi = 1.9\,\mathrm{GHz}$. Comparing this result with the renormalized resonator frequency $\omega_A/2\pi = 4.9\,\mathrm{GHz}$ we obtain a coupling fraction of $g/\omega_A \approx 0.39 > 0.3$, which is in the non-perturbative USC regime (see Sec. 1.2).

The design presented here assumes that the coupling inductance and the Josephson junction currents are perfectly on target. However, from a fabrication point of view it is challenging to obtain the exact design values and thus it is advisable to have some tolerance in the area A, current density J_c and coupling inductance L_c. In Fig. 4.7, we show the value obtained for g/ω_A as a function of J_c and L_c. The black lines indicate the region where the system is in the non-perturbative USC regime. For values of J_c and/or L_c significantly above target, we should still be able to reach $g/\omega_A > 0.3$.

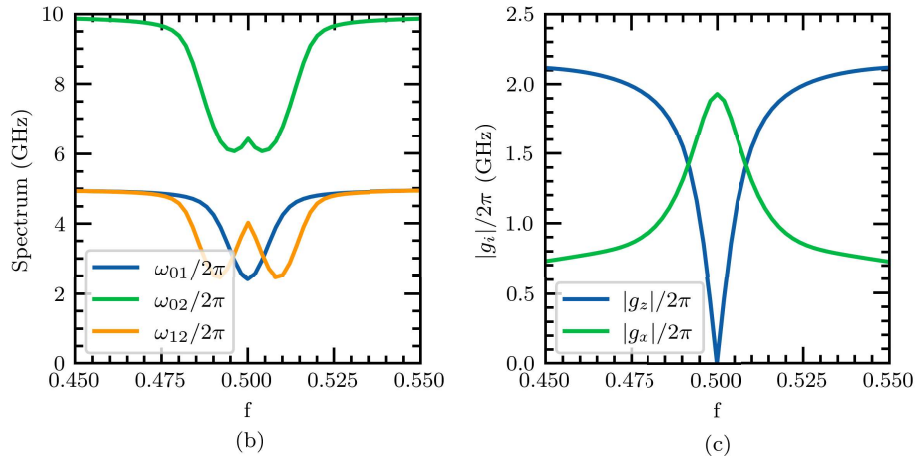

Figure 4.6: Simulated spectrum (a) and coupling coefficient (b) for the qubit-resonator design. The parameters used for the simulation are: $L_\mathrm{R} = 0.9\,\mathrm{nH}$, $C_\mathrm{R} = 740\,\mathrm{fF}$, and the qubit parameters listed in Table 4.2.

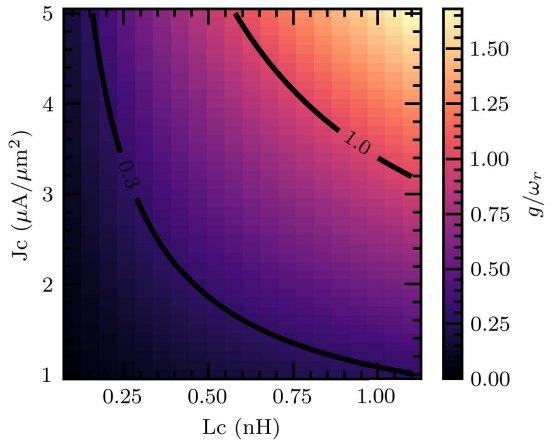

Figure 4.7: Coupling coefficient as a function of the junction current density J_c and the coupling inductance L_c. The simulation to obtain g uses the design parameters: $L_\mathrm{R} = 0.9\,\mathrm{nH}$, $C_\mathrm{R} = 742\,\mathrm{fF}$, and the qubit parameters listed in Table 4.2.

4.2 Spectrum characterization

Multiple devices have been fabricated using the recipes described in Ch. 3. Most of them suffered problems on the last fabrication step. It was latter realized that PMGI leaves a significant amount of residues which result in a lower I_c while affecting the quality of the contacts. This is the reason why we opted to replace PMGI by PMMA in the last EBL step. Furthermore, the multi-layer fabrication and the delicate structures turn out to a low fabrication yield. Nonetheless, one of the devices had a combination of off-target values that made it still suitable to validate the design and prove the grAl concept. In this section, we present the initial room-temperature and low-temperature characterization of this working device.

4.2.1 Room temperature and grAl characterization

The design of the chip contains a set of test junctions and grAl test structures that can be probed at room-temperature and low-temperature to estimate J_c and L_c.

The average resistance of junctions at room-temperature after a final bake at 200 °C for 7 min is $R_{JJ} = (5.2 \pm 0.1)\,\mathrm{k\Omega}$. The critical current of the junctions is estimated by the Ambegaokar-Baratoff formula [Amb+63] presented in Sec. 2.1.3, leading to a value of $I_c = (55.3 \pm 0.9)\,\mathrm{nA}$ for the big junctions. On the other hand, the areas of the Josephson junctions were estimated by imaging them using a scanning electron microscope (SEM). The estimated area for the big junctions is $A = (0.084 \pm 0.001)\,\mu\mathrm{m}^2$, while the small ones show $A = (0.045 \pm 0.001)\,\mu\mathrm{m}^2$, leading to $\alpha = 0.54 \pm 0.01$. The resulting Josephson and charging energies for the big junctions are $E_J/h = (27.5 \pm 0.5)\,\mathrm{GHz}$ and $E_C/h = (4.6 \pm 0.1)\,\mathrm{GHz}$, respectively, where in the later case we have used $S_c = 50\,\mathrm{fF}/\mu\mathrm{m}^2$.

The length of the grAl coupler is designed to be 30 µm and use SEM images to extract its width, $(487 \pm 15)\,\mathrm{nm}$. The room temperature resistance of the wire is extracted by measuring one of the test structures, giving $R_{RT} = (0.96 \pm 0.01)\,\mathrm{k\Omega}$. Using the design length of the coupler and the nominal thickness of the film 50 nm, we can extract the room-temperature resistivity of the grAl line, $\rho_{RT} = (78.3 \pm 2.5)\mu\Omega\,\mathrm{cm}$.

The kinetic inductance of grAl is estimated using the limit to the Mattis-Bardeen formula (2.1) introduced in Sec. 2.1.3,

$$L_k = 0.18\frac{\hbar R_{4K}}{k_B T_c}. \tag{4.5}$$

where R_{4K} is the normal state resistance measured at 4 K and T_c is the critical temperature of grAl. In order to extract T_c and R_{4K}, we wirebond one of the test

structures in a 4-probe configuration and measure current-voltage (IV) curves in temperature. We use the different IV curves to extract the resistance as a function of temperature $R(T)$. These measurements are performed on a dry dilution refrigerator fridge where the temperature is controlled manually below 4 K by adding small amounts of He^3/He^4 mixture while adjusting the heaters. For low temperatures, approaching T_c, we set low enough currents and we adjust the repetition rate of the measurement to avoid excessive heat dissipation when the sample is in the normal state. More details on critical temperature measurements can be found in Ch. 5. The resulting $R(T)$ curve for one of the grAl test structures mimicking the coupler is shown in Fig. 4.8. We define the critical temperature as the point where the resistance has decreased 50% respect to the onset value. The temperature difference between the points where the resistance has decreased a 10% and 90% of the onset value define the width of the transition. Following these definitions, we estimate the critical temperature of the grAl coupler to be $T_c = (1.60 \pm 0.31)$ K.

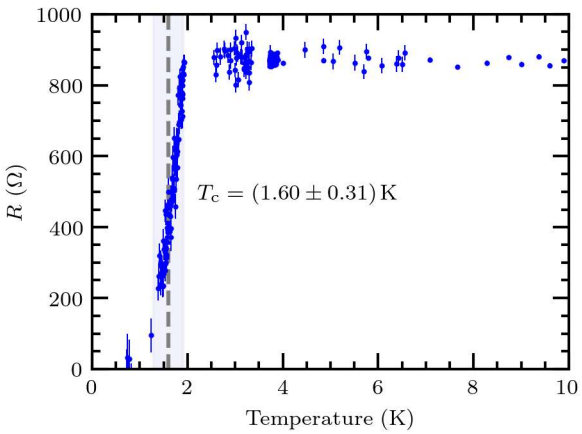

Figure 4.8: Resistance versus temperature curve for the grAl coupler test structure. The dashed vertical line indicates the point where the resistance has dropped 50% of the onset value while the shadowed area indicates the width of the transition.

Using the value of resistance obtained at 4 K, $R_{4K} = (0.86 \pm 0.01)\,k\Omega$ and the critical temperature $T_c = (1.60 \pm 0.31)$ K, we estimate the inductance of the grAl coupler to be $L_c = (0.74 \pm 0.14)$ nH, which is significantly above the target 0.5 nH of the design, yet still allowing the device to be in the USC regime.

Figure 4.9 shows the resulting estimated qubit-resonator spectrum and energy ladder using $L_c = 0.74$ nH, $A = 0.084\,\mu m^2$, $\alpha = 0.54$ and $I_c = 55.3$ nA.

The expected coupling coefficient obtained using the estimated parameters is $g/2\pi \approx 0.67\,\mathrm{GHz}$ and $g/\omega_A \approx 0.15$, where we have used the renormalized resonator frequency $\omega_A/2\pi = 4.56\,\mathrm{GHz}$. The coupling is still sufficiently large to enter in the perturbative USC regime. In addition to the qubit-resonator spectrum, we can estimate qubit parameters. Simulating a Csh 3JJ flux qubit with non-negligible loop inductance given by L_c and the parameters given above, we obtain $I_\mathrm{p} = 19.63\,\mathrm{nA}$ and $\Delta_\mathrm{q}/h = 4.71\,\mathrm{GHz}$ for the qubit. Note that the expected qubit persistent current is more than 3 times smaller than the design value. Nevertheless, such a low current indicates a potentially more coherent device.

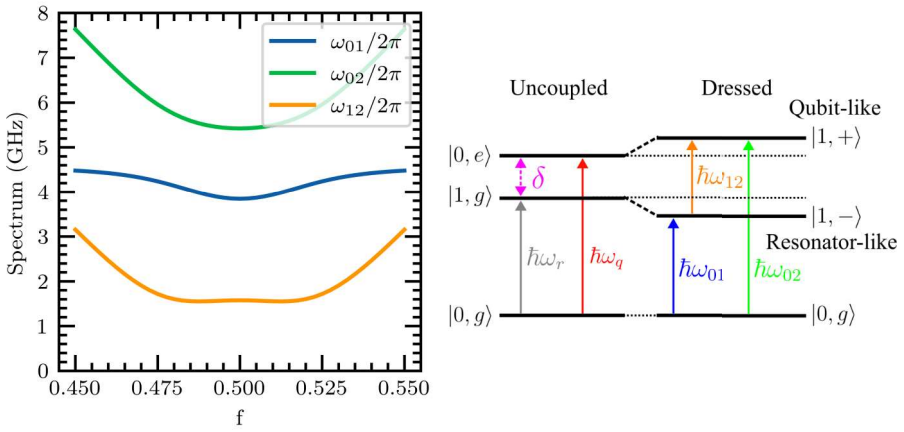

Figure 4.9: Estimated spectrum and energy ladder for the qubit-resonator system. Left: qubit-resonator spectrum obtained using the estimated values at room temperature of the grAl kinetic inductance L_c, junction current density J_c and junction areas A. The resonator parameters used are $L_\mathrm{R} = 0.9\,\mathrm{nH}$ and $C_\mathrm{R} = 0.74\,\mathrm{pF}$. Right: schematics of energy ladder near the sweetspot for the estimated spectrum presented on the left panel. In the perturbative USC regime, the states of the system can be expressed as dressed states $\{|1,+\rangle, |1,-\rangle\}$ of even and odd superpositions of the uncoupled qubit-resonator states $\{|n-1,e\rangle, |n,g\rangle\}$ with a perturbative effect of the counter-rotting terms [For+16]. The term resonator(qubit)-like indicates that the dressed state has a predominant component of the bare resonator (qubit) state.

4.2.2 Low-temperature transmission measurements

Figure 4.10 shows a false-colored image of the completed device. The chip is packaged in a copper sample box with a coil to tune the flux through the qubit

loop. The sample is then mounted on the base-temperature plate of our dilution refrigerator with input/output connections on either one of the feedlines since we have one cold amplifier. The rest of the ports are terminated with a 50 Ω termination.

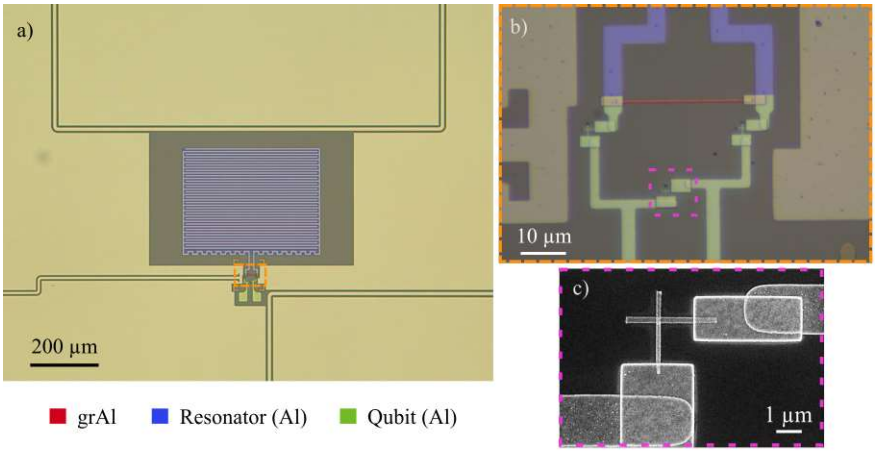

Figure 4.10: False colored images of the device. (a) shows the complete qubit-resonator system with the different feedlines, (b) is a zoom into the qubit loop and (c) is a SEM image of the small junction of the device.

We measure the sample in transmission using a single-tone measurement technique as described in Sec. 2.2. Using a Vector Network Analyzer (VNA), we scan with a tone at frequency f_{sys} while monitoring the transmission. The different resonant frequencies of the system appear as dips in $|S_{21}|$. Thanks to the layout of the device, we can run this measurement independently through the resonator (S_{21}^{R}) or the qubit (S_{21}^{Q}) feedline. In Fig. 4.11, we show the resulting transmission spectrum of the system through (a) resonator and (b) qubit feedline as a function of the external flux. The magnitude of the transmission is normalized as,

$$|S_{21}^{\text{norm}}(f_i, \Phi_{\text{ext}})| = \{|S_{21}(f_i, \Phi_{\text{ext}})| - \min(|S_{21}(f_i, \Phi_{\text{ext}})|)\} / \text{std}(|S_{21}(f_i, \Phi_{\text{ext}})|)$$

where f_i is the frequency at each trace. The signal is normalized to eliminate spurious box modes which offset the vertical range.

In both measurements, we observe two main transitions, one between 4 and 4.5 GHz and another one between 6 and 8 GHz. The lower one (ω_{01}) has more resonator-like component, while the higher transition (ω_{02}) is mostly related to the qubit. This information can be extracted from the mode analysis of the estimated spectra of the circuit (Fig. 4.9). Additional features appear at flux

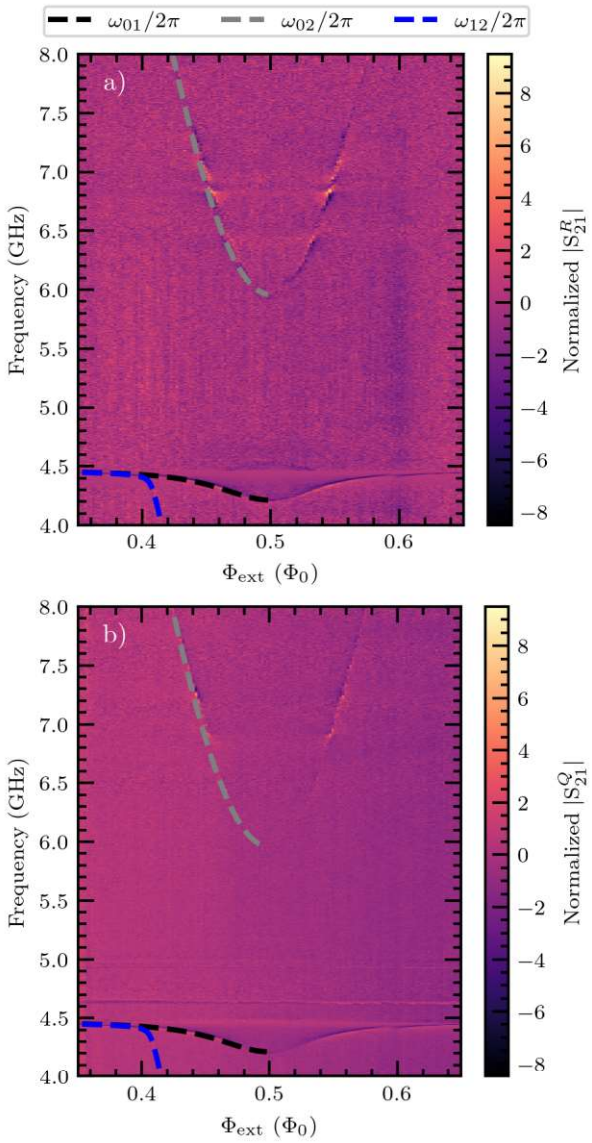

Figure 4.11: Normalized transmission magnitude vs. flux bias (Φ_{ext}) obtained via single-tone spectroscopy. The dashed lines correspond to the fitted Quantum Rabi Model spectrum with fit parameters Δ_{q}, I_{p} and g. See the main text for more details. a) Spectrum obtained measuring through the resonator feedline. b) Spectrum obtained measuring through the qubit feedline.

$\Phi_{\text{ext}}/\Phi_0 \sim 0.4$ and 0.6 which come from intermediate transitions such as ω_{12}. The identification of the different transitions will be further investigated with two-tone spectroscopy measurements discussed in following sections.

From the theory derived in [Mag+21], we expect significant differences in the transmission spectra when probing the system through qubit or resonator. In particular, one should expect the resonator-like transition to vanish outside the sweetspot when probing the system through the qubit feedline and, the qubit-like transition to be dimmer when the system is probed through the resonator. Instead, in our experiment, although $|S_{12}^R|$ for ω_{01} is $\sim 5\,\text{dB}$ dimmer than $|S_{21}^Q|$, we do not see the signal disappear for flux $\Phi_{\text{ext}}/\Phi_0 < 0.45$ and $\Phi_{\text{ext}}/\Phi_0 > 0.55$. In Fig. 4.12, we show the raw $|S_{21}|$ data around 4.5 GHz where the signal is comparable in both measurements. Note that one of the spurious box modes at 4.36 GHz is not present in the qubit measurement. We took advantage of the fact that the measurements were performed in different cooldowns, and we included a copper piece inside the sample box to fill in empty space and bring box modes to higher frequencies (see Sec. 2.2 for more details). Similarly to the first transition, the $|S_{21}|$ signal at ω_{02} is comparable for both measurement configurations. In this region of the spectrum, it is very difficult to give a quantitative difference on the transmission magnitude due to the low signal (see Fig. 4.13). The differences between theory and experiment could come from either an over-coupling of the qubit/resonator to the feedline or a stray crosstalk between lines.

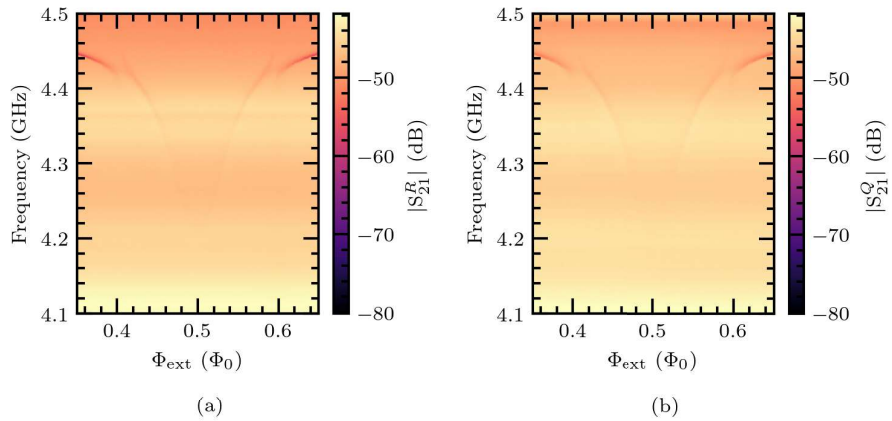

Figure 4.12: Raw $|S_{21}|$ data around 4 GHz obtained by probing the system through (a) resonator and (b) qubit feedline as a function of the external flux.

We simulate in *Sonnet* the qubit-resonator system with both feedlines to understand the small differences between the single-tone spectra presented in

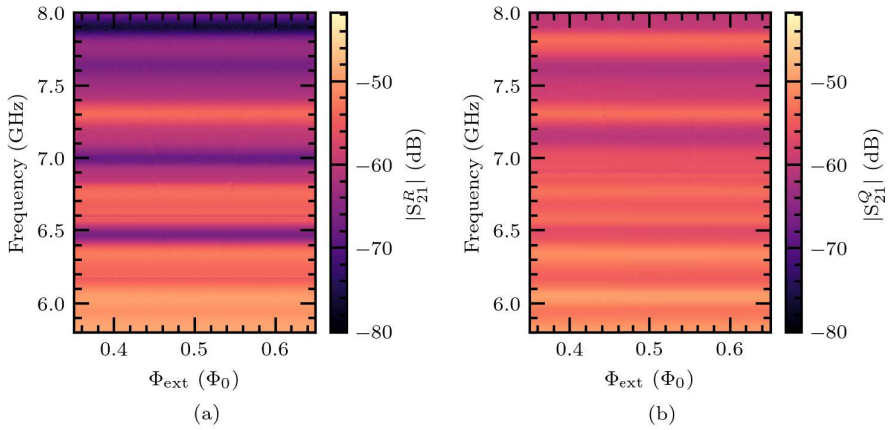

Figure 4.13: Raw $|S_{21}|$ data between 5 GHz and 8 GHz obtained by probing the system through (a) resonator and (b) qubit feedline as a function of the external flux.

Fig. 4.11. The schematics of the simulation is shown in Fig. 4.14. We start by simulating the resonator coupled to the qubit by an ideal inductor with $L_c = 0.74\,\text{nH}$. In order to simulate the qubit, we remove the Josephson junctions of the design, keep the C_{sh} capacitor, and use ideal inductor and capacitor elements to mimic the qubit resonance frequency at the sweetspot. For both feedlines (see left panels in Fig. 4.15) we observe a resonance centered at 4.45 GHz with a magnitude which is $\sim 4\,\text{dB}$ smaller in the qubit feedline case. The crossed signal S_{14} between feedlines is in general below $-10\,\text{dB}$, with a peak around 4.45 GHz which is compatible with the excitation of the resonator. The $\sim 4\,\text{dB}$ difference between $|S_{21}|$ and $|S_{43}|$ in the simulations is consistent with the one observed in the experiments between $|S_{21}^{\text{Q}}|$ and $|S_{21}^{\text{R}}|$ ($\sim 5\,\text{dB}$). On the other hand, given the low crossed signal S_{14}, the direct crosstalk between feedlines is at a level of $-25\,\text{dB}$.

To discard that the coupling between qubit feedline and resonator comes directly from the C_{sh}, we perform a second simulation consisting of removing completely the qubit loop and the C_{sh} capacitor. In addition to focusing on the different resonances, we analyze the currents of the simulation. In the central panels of Fig. 4.15, we observe that even though the qubit parts are not present in the simulation, the resonator resonance is still present when probing the system through the qubit feedline (S_{21}). An analysis of the currents indicates that the open ground plane around the bottom feedline provides a current path through the ground towards the resonator inductor. These stray currents provide a direct

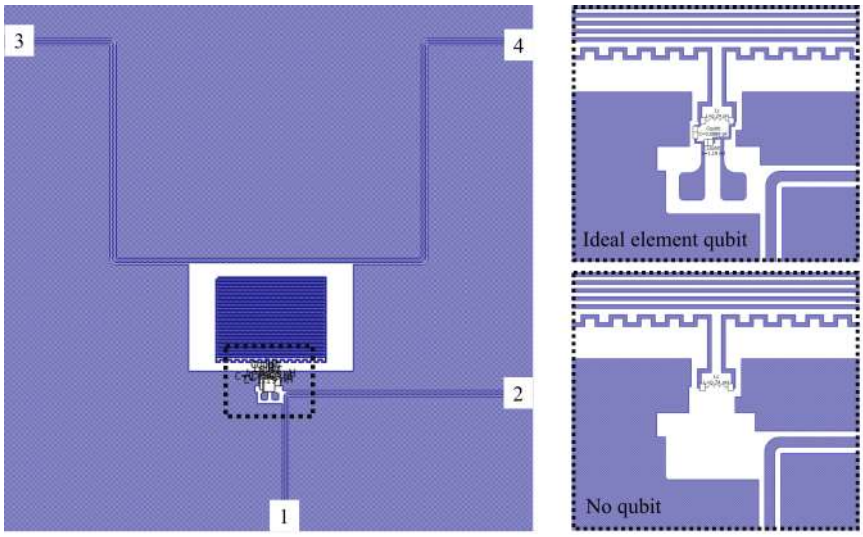

Figure 4.14: *Sonnet* simulation layout. The left panel provides the port labels for both feedlines. The right panels are an enlarged view around the qubit loop for a qubit simulated out of ideal elements (top), and a simulation without qubit loop (bottom).

coupling between the qubit feedline and the resonator which could explain the similar transmission in Figs. 4.11 a), b).

The coupling of the resonator to the qubit feedline may be minimized by closing the ground plane surrounding it. There are two possibilities; the first is to modify the lithography design and connect the two sections with an Al line, and the second one consists of including an air bridge. We test both solutions in *Sonnet* and simulate the resonator without qubit. In both cases, the currents through the ground edges are significantly reduced and $|S_{21}|$ is now practically unmodified around the resonance frequency of the resonator. Therefore, by connecting both ground planes, the stray coupling of the resonator to the qubit feedline is canceled. This will be considered in future device designs.

Coupling estimate

Using the data obtained via single-tone spectroscopy, we extract the frequency values corresponding to the lowest transition labeled ω_{01}. We use these values to perform a two-tone spectroscopy measurement. We send a tone at ω_{01} while scanning in frequency with another tone at f_{sys}. When f_{sys} excites one of the

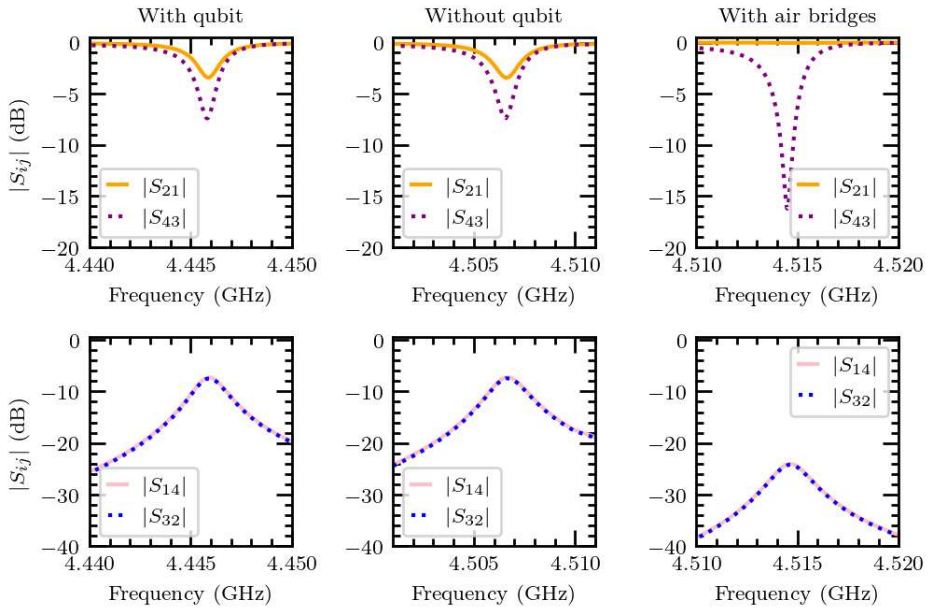

Figure 4.15: $|S_{ij}|$ for different *Sonnet* simulations with two feedlines. $|S_{21}| = |S_{21}^{Q}|$, $|S_{43}| = |S_{21}^{R}|$, and $|S_{14}|$ and $|S_{32}|$ are the crossed signals between resonator and qubit feedlines. Left panel: simulation with ideal element qubit. Central panel: simulation without qubit and C_{sh} capacitor. Right panel: simulation without qubit and C_{sh} capacitor where the ground planes are connected by air bridges.

transitions of the system, it produces a shift in ω_{01} and we observe a change in transmission. This process is repeated for different external flux values. The resulting normalized spectrum is shown in Fig. 4.16.

We identify four out of the five transitions visible in the spectrum. ω_{01} is mostly related to the resonator and it is the transition used to measure in the two-tone configuration, while ω_{02} has more qubit component. The intermediate transition ω_{12}, which is also visible using single-tone spectroscopy, and a two-photon transition to ω_{03}. One spectral line, indicated with a black arrow in Fig. 4.16 around 5 GHz and $\Phi_{\mathrm{ext}}/\Phi_0 = 0.36$, seems to match a type of three-photon blue-sideband transition with $\hbar(\omega_{01} + \omega_{03})/3$.

In order to extract the system parameters, we fit the visible transitions in single-tone and two-tone spectroscopy to the Quantum Rabi Model (3.18) pre-

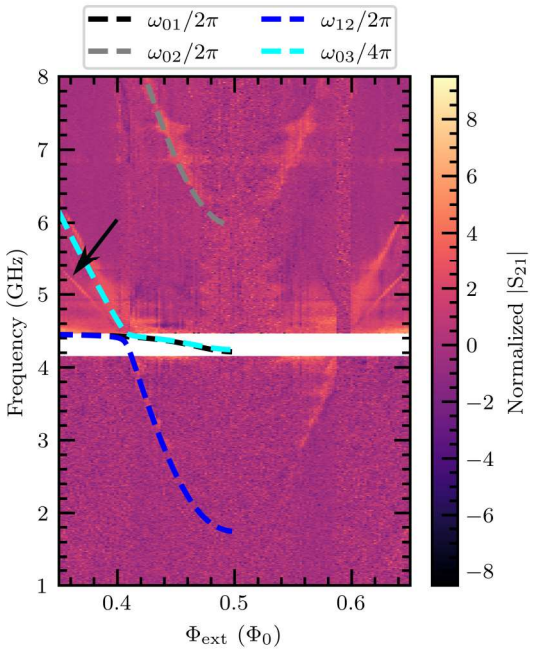

Figure 4.16: Normalized transmission magnitude vs. flux bias (Φ_{ext}) obtained via two-tone spectroscopy using the qubit feedline. The resonator tone is fixed at the frequencies defined by the ω_{01} transition measured using single-tone spectroscopy. The dashed lines correspond to the fitted Quanutm Rabi Model spectrum with fit parameters Δ_{q}, I_{p} and g. The arrow indicates the three photon process described in the main text.

sented in Ch. 3,

$$\hat{\mathcal{H}}_{\text{QRM}} = -\frac{1}{2}\left(\epsilon\hat{\sigma}_z + \Delta_{\text{q}}\hat{\sigma}_x\right) + \hbar\omega_r\left(\hat{a}^\dagger\hat{a} + \frac{1}{2}\right) + \hbar g\hat{\sigma}_z\left(\hat{a} + \hat{a}^\dagger\right), \tag{4.6}$$

where $\epsilon = 2I_{\text{p}}\left(\Phi_{ext} - \frac{\Phi_0}{2}\right)$. We implement a *least-squares fitting* with the package *iminuit*[5] that fits ω_{01}, ω_{02}, part of ω_{12} and $\omega_{03}/2$ simultaneously. The resulting values of the fit read $I_{\text{p}} = (11.619 \pm 0.004)\,\text{nA}$, $\Delta_{\text{q}}/h = (5.707 \pm 0.002)\,\text{GHz}$, $g/2\pi = (0.578 \pm 0.001)\,\text{GHz}$ and $\omega_r/2\pi = (4.463 \pm 0.001)\,\text{GHz}$. The frequency of the resonator mode is also independently obtained by measuring in transmission at high powers. For high enough power, the qubit saturates (similarly to a

[5]https://scikit-hep.org/iminuit

punch-out measurement [Ree+10]) and ω_{01} does not change in flux. This saturated transition corresponds to the renormalized LC resonator frequency ω_r. The measured frequency using this procedure is $\omega_r/2\pi = 4.465\,\mathrm{GHz}$, which is compatible with the fitted parameter.

From the resulting fitted parameters we estimate the strength of the interaction, $g/\omega_r \simeq 0.13 > 0.1$. The coupling still falls in the perturbative USC regime despite the small persistent current of the qubit. The result is consistent with the repulsion between levels observed near the qubit sweet-spot as well as the multiple spectral lines observed by single-tone spectroscopy. The coupling of the system could easily be increased by designing larger coupling inductors. This result opens the door to studying flux qubits with low persistent currents in the USC regime using superinductor materials as couplers, potentially leading to a highly coherent system in the USC regime.

4.2.3 USC spectrum discussion

In this section, we present the main spectral features of the measured qubit-resonator system and we discuss some visible USC features.

Comparison with the Jaynes-Cummings model

In the previous section, we have concluded that the qubit-resonator coupling satisfies the condition $g/\omega_r > 0.1$. This implies that the system is in the ultrastrong coupling regime and the effect of counter-rotating terms is non-negligible. This effect can be quantified by the Bloch-Siegert shift (ω_{BS}) which is given by the difference between the Jaynes-Cummings (JC) spectrum and the Quantum Rabi model spectrum [For+10]. As seen in Fig. 4.17, the resonator experiences a downward shift respect to the JC spectrum. The shift is maximal at the sweetspot, corresponding to the region of maximal qubit-resonator coupling.

Figure 4.18 shows the data corresponding to the ω_{01} transition together with the QRM fit and the resulting JC spectrum using the QRM fitting parameters. The orange data points are extracted by fitting S_{21}^{R} to the resonator model from [Pro+15] (see Sec. 5.4.2 for more details on resonator fitting). The error-bars are given by the extracted linewidth of the transition. The signal at the sweetspot is very low and the resonator fitting fails. For this region (blue points) we extract the data as the minima of the normalized $|S_{21}^{R}|$. The error bars are an estimate of the linewidth based on the normalized spectra. As expected, the JC model predicts a higher resonance frequency at the sweetspot. The right panel of Fig. 4.18 allows us to quantify the Bloch-Siegert shift. We show the difference between the QRM and the JC model $\omega_{01}^{\mathrm{QRM}} - \omega_{01}^{\mathrm{JC}}$, and the difference between the dataset and the JC model $\omega_{01} - \omega_{01}^{\mathrm{JC}}$. As previously anticipated, the difference between the QRM and the JC is maximum at the sweetspot with a value of $\sim 23\,\mathrm{MHz}$

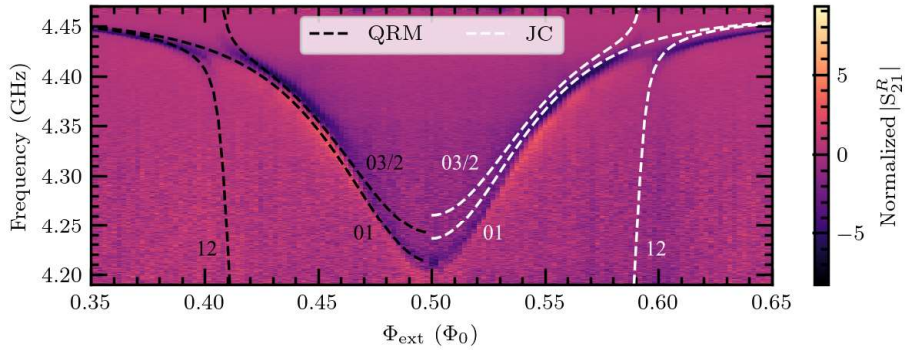

Figure 4.17: Zoom around the ω_{01} transition. In black we show the fitted QRM spectrum and in white the calculated JC spectrum using the QRM fitting parameters.

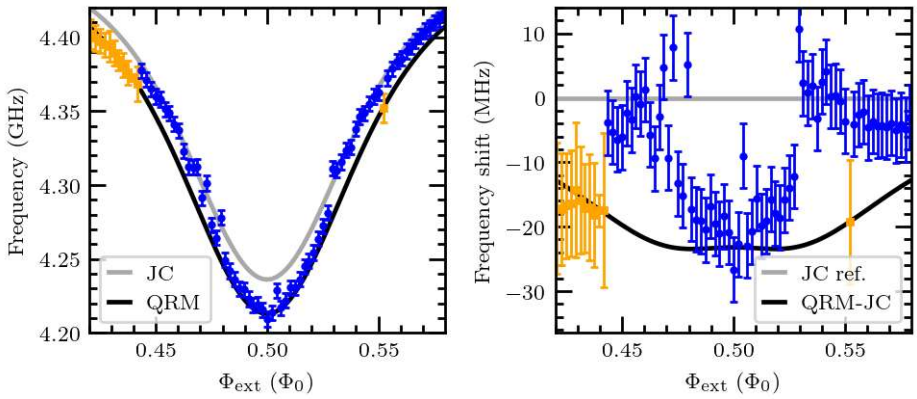

Figure 4.18: Comparison between the QRM fit and the JC model near the sweetspot for the lowest transition, ω_{01}. Left panel: comparison between QRM and JC models, in orange data points extracted via resonator fit on S_{21}^R, in blue data points extracted as the minima of $|S_{21}^R|$ normalized. In black we show the fit to the QRM and in gray the calculated JC spectrum using the fitting QRM parameters. Right panel: extraction of the resonator shift by subtracting the JC spectra to the data points and QRM spectra shown in the left panel. The difference is the Bloch-Siegert shift, with a maximum at the sweetspot of $\omega_{BS}/2\pi = 23\,\text{MHz}$.

for the ω_{01} transition. This difference corresponds to the Bloch-Siegert shift $\omega_{BS} = g^2/(\omega_r+\omega_q)$. We can use this shift to estimate the coupling coefficient. At the sweetspot, $\omega_{BS}/2\pi = 23\,\mathrm{MHz}$, $\omega_r/2\pi = 4.463\,\mathrm{GHz}$ and $\Delta_\mathrm{q}/h = 5.707\,\mathrm{GHz}$, we obtain a coupling coefficient $g \simeq 0.48\,\mathrm{GHz}$ and a fraction $g/\omega_r \simeq 0.11$, which is consistent with the QRM fitted parameters.

Comparison with the expected spectrum

In Sec. 4.2.1, we have presented the estimated spectrum of the system obtained using the parameters derived from resistance measurements both at room-temperature and at low-temperature. The initial coupling strength estimate was $g/\omega_r \simeq 0.15$ which is not far from what we obtained in the experiment, $g/\omega_r \simeq 0.13$. Still, there are significant differences in the spectra. Figure 4.19 shows the expected (solid) and fitted QRM (dashed) spectrum.

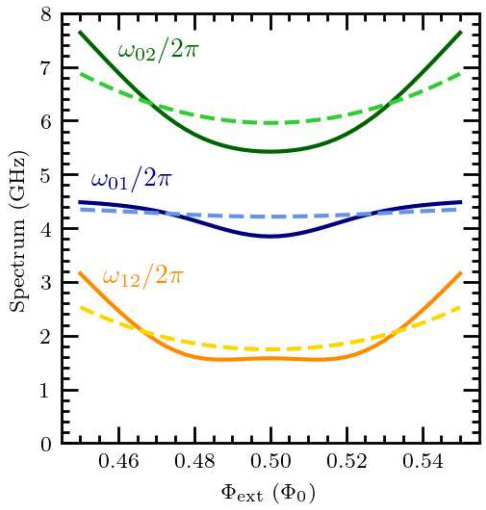

Figure 4.19: Comparison between the expected (solid) and fitted QRM (dashed) qubit-resonator spectrum obtained using the parameters listed in Table 4.3.

There is a considerable difference in the curvature of ω_{02} between expected and fitted spectra, which indicates a difference in qubit persistent current. In fact, there is almost a factor two difference (see Table 4.3 for a summary of the expected and fitted parameters). Similarly, the difference in qubit gap is 1 GHz which explains the bigger change in ω_{01} around the sweetspot for the expected spectrum.

Table 4.3: Summary of expected and fitted spectrum parameters. The expected parameters are extracted from room-temperature measurements and low-temperature resistance measurements, while the fitting parameters are obtained fitting the qubit-resonator spectrum to the QRM.

	I_p (nA)	Δ/h (GHz)	$\omega_r/2\pi$ (GHz)	$g/2\pi$ (GHz)
Expected	19.63	4.72	4.56	0.67
Fitted	11.619 ± 0.004	5.707 ± 0.002	4.463 ± 0.001	0.578 ± 0.001

The differences between expected and fitted spectra can be explained by deviations in the estimated qubit parameters. For example, we used the area of junctions fabricated in neighboring chips, but this does not warrantee that the junctions of the measured qubit are the same. Similarly, we used the resistance at room-temperature to estimate the critical current of the junction. However, the room-temperature resistance of the junction can be significantly different from its the normal state resistance. Finally, we set the design parameters for the different qubit capacitances which might differ from the actual value. Recall that C_J is calculated from $S_\mathrm{c} = 50\,\mathrm{fF}/\mu\mathrm{m}^2$, which is an estimated parameter. Additionally, small deviations in the dimensions of the shunted capacitor pads may also lead to differences between the designed and real value of C_sh

Even though the expected qubit parameters were off-target, the resonance frequency of the resonator was quite similar to the one of the measured device. This tells us that the coupling inductor estimate was close to the actual value. The 100 MHz difference to the measured value could be due to the use of design parameters L_R and C_R, or to inhomogeneities of grAl across the chip. Finally, we can compare the designed loaded quality factor of the resonator with the extracted one by fitting S_{21}^R far from the sweetspot. For $f = 0.28$ we extract $Q_\mathrm{L} \simeq 1000$ which is 5 times lower than the design value. The difference may come from the stray couplings to the qubit feedline, as discussed in Sec. 4.2.2.

4.3 Outlook

Although the results presented in the previous section are promising, several improvements can be made in the design to yield a mode robust experiment:

- Verify the absence of cross-talk between feedlines by measuring variations of the device presented in previous sections. One copy should contain only one feedline coupling either to qubit or resonator.

- Characterize the limitations imposed by the qubit feedline. The goal is to determine a minimal coupling to the feedline such that the qubit coherence

is not limited by this loss channel. This can be addressed by designing a qubit coupled to a modified resonator with very high frequency. The L_R is kept identical to the original design to consider for the renormalization of the qubit spectrum.

With this in mind, we propose variations of the device presented in Sec. 4.1. The goal of this new generation of devices is to discard crosstalk between feedlines and understand better the readout of the system through the qubit. The three proposed devices are shown in Fig. 4.20. The first copy represents a control for the complete experiment. The second copy does not contain the qubit feedline, and the third one only contains the qubit feedline and the capacitance of the resonator is modified to yield a resonator with a resonance frequency well above 8 GHz. This third configuration will be used to study single qubit scattering.

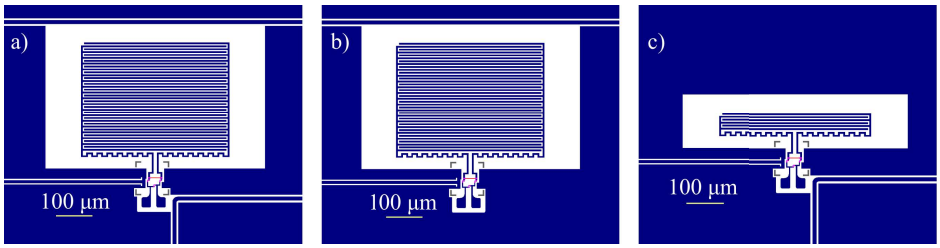

Figure 4.20: Desing variations for the new generation of devices. (a) old design containing two feedlines; (b) design with only the resonator feedline (c) design with the modified resonator capacitance and a single feedline coupling to the qubit to study single qubit scattering.

In these new devices we include test structures to probe the grAl and Josephson junctions in intermediate steps of fabrication. In Fig. 4.21 we show the different test structures designed for the new generation. Structures (a) and (b) were already present in the old design and they mimic the final structures in the chip. Structures (c) and (d) are an adapted single-layer version of the previous two. These new structures will allow us to adjust the parameters after each fabrication step to ensure that the final chip is in the non-perturbative USC regime.

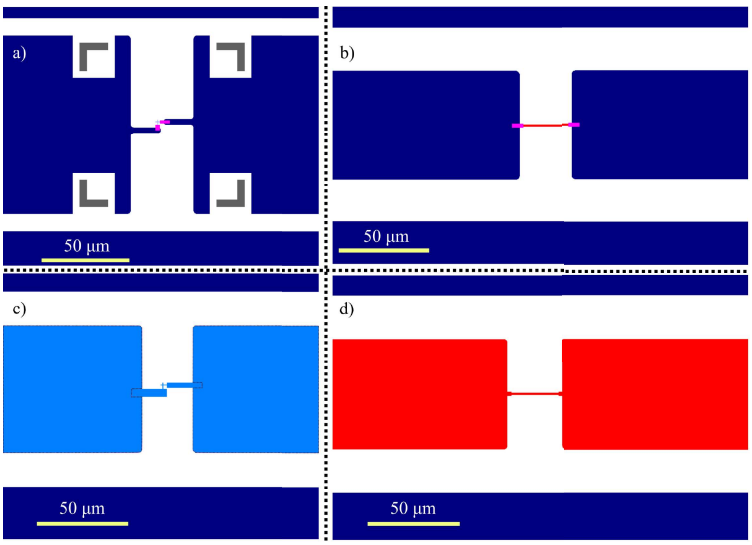

Figure 4.21: On-chip test structures: (a) test junctions with contacts (old); (b) grAl test line with contacts (old); (c) test junctions to be fabricated on a single EBL step (new); (d) grAl line to be fabricated on a single EBL step (new).